Bridging scales in non-standard thermo-viscoelastic periodic materials via dynamic non-local homogenization

February 20, 2026

Abstract

This study aims to develop a new framework for analysing the dynamic response of thermo-viscoelastic heterogeneous materials with periodic microstructure. To this end, a non-local asymptotic homogenization formulation designed to capture the influence of microstructural features on wave propagation is introduced. The approach is built upon a compact matrix-operator representation that facilitates the definition of the cell problems and the associated down-scaling relation, from which average field equations of infinite order are derived and structured according to increasing powers of the microstructural characteristic size. A central objective of the method is to obtain accurate dispersion relations in the frequency–wavenumber domain by evaluating these equations at different approximation orders. In doing so, the framework successfully reconstructs both the low-frequency acoustic branch and the onset of the first optical branch at higher frequencies, thus providing a precise description of the material's complex spectrum. The validity of the formulation is demonstrated through direct comparison with the Floquet–Bloch spectrum of the heterogeneous medium, yielding excellent agreement. Furthermore, the method is conceived to be versatile and can be applied to a broad range of periodic microstructural configurations.

Keywords: thermo-viscoelastic periodic materials, asymptotic homogenization, constitutive identification, damped wave propagation

1 Introduction

The behavior of materials subjected to coupled thermal and mechanical actions is classically described by the theory of thermoelasticity, where temperature variations and mechanical strains are intrinsically coupled through energy conversion mechanisms. In this framework, thermomechanical loadings induce an exchange between mechanical and thermal energy, resulting in both deformation and temperature changes within the body. However, many engineering and biological materials exhibit a pronounced time-dependent response, leading to mechanical energy dissipation and temperature-dependent deformation. This broader class of phenomena is addressed by thermo-viscoelasticity, which extends the standard theory to incorporate both hereditary effects and non-Fourier heat conduction. Such generalizations become essential when dealing with amorphous solids, colloids, glassy systems, or porous media, for which classical Fourier-based models fail to capture characteristic relaxation mechanisms [1–3]. Thermo-viscoelastic behavior is especially relevant in polymers, composites, and biological tissues, widely used in applications ranging from additive manufacturing and flexible electronics to biomechanics and civil engineering [4–9]. Numerous studies have therefore focused on developing constitutive models capable of capturing these complex responses, whether at the continuum level, e.g., bio-thermo-mechanical modeling of soft tissues [10], nonlinear thermomechanical behavior of polymer composites [11, 12], or efficient formulations for surgical simulation [13], or at the microscale, where the intrinsic heterogeneity of composite materials must be explicitly taken into account [14–16]. Experimental studies supporting these modeling efforts further highlight the strong coupling between temperature, deformation rate, and relaxation phenomena [5].

Given the multiscale nature of thermo-viscoelastic composites and the scale separation often present between microstructural length and overall dimensions, homogenization techniques play a central role in deriving effective macroscopic descriptions. Besides the micromechanical modelling [17, 18], given the validity of

the scales separation hypothesis, homogenization approaches serve as effective tools for establishing the overall static and dynamic properties of an equivalent continuum, overcoming the computational effort of deriving the response of the heterogeneous material characterized by rapidly oscillating coefficients. To analyse the response of elastic materials, the most developed strategies include the asymptotic, the variational-asymptotic, and the computational approaches [19–29]. Such methods have also been extended to treat the effects of multi-field coupling on the dynamic response of periodic materials [30–33]. Several studies have extended homogenization techniques to thermoelastic and thermo-viscoelastic media, developing variational-asymptotic frameworks for periodic and complex materials within the framework of non-standard thermoelasticity, considering either single or multiple thermal relaxation times. These approaches enable the analysis of wave propagation, multi-field coupling, and scale-dependent effects, providing effective macroscopic descriptions of heterogeneous materials [34, 35]. The formulation in [36] incorporates temperature-dependent viscoelastic effects in fiber-reinforced composites by modelling elastic fibers within a viscoelastic matrix. Multi-scale homogenization strategies have also been employed to characterize the time-dependent thermal expansion of 3D woven composites [37, 38] and to derive thermo-viscoelastic constitutive laws for unidirectional fiber-reinforced plastics [39]. Further contributions include procedures for predicting temperature-dependent macroscopic expansion coefficients [40], numerical homogenization of viscoelastic responses in woven composites [41], and two-scale analyses of curing processes in composite laminates [42]. Finally, [43] proposed a multiscale thermo-viscoelastic model to assess residual stress development in thermoset composites by representing the laminate as a stack of homogeneous layers.

Building on these foundations and motivated by the significant role of thermo-viscoelasticity in modern material systems, the present study introduces a new non-local asymptotic homogenization framework specifically tailored to periodic thermo-viscoelastic materials, assuming that the heat flux follows the hereditary integral relying on the gradient of temperature in the time domain.

Nomenclature

Symbol	Meaning
$\boldsymbol{x}$	position vector
t	time coordinate
s, ω	complex frequency, angular frequency
$\boldsymbol{\zeta}$	translation variable
$\boldsymbol{k}$	wavevector
$\boldsymbol{\sigma}(\boldsymbol{x},t)$	stress tensor
$\boldsymbol{\varepsilon}(\boldsymbol{x},t)$	strain tensor
$\mathbb{G}^m(\boldsymbol{x},t)$	elasticity relaxation tensor
$\boldsymbol{\psi}^m(\boldsymbol{x},t)$, $\tilde{\boldsymbol{V}}^m(\boldsymbol{x},t)$, $\tilde{m}^m$	relaxation form of thermal dilatation, heat conduction tensors and constant
$\boldsymbol{u}(\boldsymbol{x},t)$	displacement field
$\boldsymbol{q}(\boldsymbol{x},t)$	heat flux vector
$\theta(\boldsymbol{x},t)$, T_0	relative temperature, reference temperature
$\rho^{(m)}(\boldsymbol{x})$, $\boldsymbol{b}(\boldsymbol{x},t)$, $\tilde{r}(\boldsymbol{x},t)$	material density, body forces, heat sources
$\boldsymbol{z}(\boldsymbol{x},t)$, $\boldsymbol{Z}(\boldsymbol{x},t)$ $\boldsymbol{g}(\boldsymbol{x},t)$	vector of unknowns at the micro and at the macro scale, vector of source terms
L, ϵ, $(\cdot)^m$	structural length, microstructural length, variable at the microscale
s_ζ	reference frequency
χ^n, $\tau_r^n(\boldsymbol{x})$	n-th viscosity ratio of the relaxation functions, n-th relaxation time
$\gamma^{(\cdot)}$, $\phi^{(\cdot)}$, $\psi^{(\cdot)}$, r_E, r_ρ, r_K, r_p	dimensionless parameters
$\mathcal{P}$, $\mathcal{U}$	periodic cell, unit cell
$\mathfrak{s}_m$, η	thickness of the m-th layer, thickness ratio
ι	imaginary unit
$\bar{(\cdot)}$	nondimensional variables
$\boldsymbol{A}^{(i,j)}$, $\boldsymbol{B}^{(h,k,y)}$	square algebraic operators, perturbation functions collector
$\mathcal{L}[\cdot]$, $\mathcal{L}^{-1}[\cdot]$	two-sided Laplace transform, inverse Laplace transform
$\hat{(\cdot)}$	transformed tensors in the Laplace domain
$\mathcal{F}_B[\cdot]$, $\mathcal{F}_B^{-1}[\cdot]$	multidimensional Floquet-Bloch transform, inverse Floquet-Bloch transform
$\mathring{(\cdot)}$	Floquet-Bloch transformed variables
$\mathcal{F}[\cdot]$, $\mathcal{F}^{-1}[\cdot]$	spatial and inverse-spatial Fourier transforms with complex argument
$\breve{(\cdot)}$	spatial Fourier transformed variables

Unlike existing formulations, the proposed method adopts a compact matrix-operator representation, enabling the derivation of average field equations of infinite order organized according to the powers of the microstructural characteristic size. By transforming these equations into the frequency–wavenumber domain, highly accurate dispersion relations are obtained at different approximation orders, capturing not only the low-frequency acoustic behavior but also the onset of the first optical branch. The formulation is validated against the complex spectrum computed through Floquet–Bloch theory for the heterogeneous material, showing excellent agreement and demonstrating the versatility of the approach across different microstructural geometries. The work is organized as follows. Section 2 introduces the microscale field equations in both the time domain and the complex-frequency domain. In this setting, the transformed equations are rewritten in a compact matrix-operator format, and the Floquet–Bloch transform is employed to analyse wave-propagation phenomena. Section 3 derives the micro-fields in the Laplace domain and develops their asymptotic expansion with respect to the characteristic length scale, leading to the formulation of the cell problems, the down-scaling relation, and the average field equations of infinite order. Free-wave propagation in thermo-viscoelastic periodic media is then examined by expressing these macroscopic equations in the frequency–wavenumber domain. Building on the idea that higher-order truncations yield increasingly accurate approximations of the complex spectrum, Section 4 validates the homogenized dispersion curves, at different approximation orders, against the analytical Floquet–Bloch solution. In the elastic limit, the method successfully captures not only the low-frequency acoustic branches but also the higher-frequency optical ones, a feature rarely addressed in previous studies. Finally, Section 5 summarizes the main findings and outlines prospective research directions.

2 Micromechanics model setting

A thermo-viscoelastic material embedded in a two-dimensional domain $\{\mathbf{O}, \mathbf{e}_j\}$ is defined by the periodic cell $\mathcal{P} = [0, \epsilon]^2$ with dimension ϵ and characterized by the periodicity vectors $\mathbf{e}_j$, with $j = 1, 2$. According to [44, 45], the constitutive equations that characterize the material are expressed in components as

$$\sigma_{ij}(\boldsymbol{x}, t) = \int_{-\infty}^{t} \Big(G^m_{ijhk}(\boldsymbol{x}, t-\tau)\dot{\varepsilon}_{hk}(\boldsymbol{x}, \tau) - \psi^m_{ij}(\boldsymbol{x}, t-\tau)\dot{\theta}(\boldsymbol{x}, \tau) \Big) d\tau, \tag{1a}$$

$$q_i(\boldsymbol{x}, t) = -\int_{-\infty}^{t} \tilde{V}^m_{ij}(\boldsymbol{x}, t-\tau) \frac{D}{Dx_j} \dot{\theta}(\boldsymbol{x}, \tau) d\tau, \tag{1b}$$

where, defining the base for a generic tensor of order n as $\mathbf{e}_{i\ldots j} = \mathbf{e}_i \otimes \ldots \otimes \mathbf{e}_j$, the components refer to the stress tensor $\boldsymbol{\sigma}(\boldsymbol{x}, t) = \sigma_{ij}(\boldsymbol{x}, t)\mathbf{e}_{ij}$, the elasticity relaxation tensor $\mathbb{G}^m(\boldsymbol{x}, t) = G^m_{ijhk}(\boldsymbol{x}, t)\mathbf{e}_{ijhk}$, which accounts for the viscoelastic effects and has major and minor symmetries, the strain tensor $\boldsymbol{\varepsilon}(\boldsymbol{x}, t) = \varepsilon_{ij}(\boldsymbol{x}, t)\mathbf{e}_{ij}$, the symmetric relaxation form of thermal dilatation tensor $\boldsymbol{\psi}^m(\boldsymbol{x}, t) = \psi^m_{ij}(\boldsymbol{x}, t)\mathbf{e}_{ij}$, the relative temperature $\theta = T - T_0$, where T_0 is the reference temperature, the heat flux vector $\boldsymbol{q}(\boldsymbol{x}, t) = q_i(\boldsymbol{x}, t)\mathbf{e}_i$ and the symmetric relaxation function form of the heat conduction tensor $\tilde{V}^m_{ij} = V^m_{ij} T_0$ with $\boldsymbol{V}^m(\boldsymbol{x}, t) = V^m_{ij}(\boldsymbol{x}, t)\mathbf{e}_{ij}$. Therefore, the balance equations related to the thermo-viscoelastic material are written into components as

$$\frac{D}{Dx_j}\sigma_{ij}(\boldsymbol{x}, t) + b_i(\boldsymbol{x}, t) - \rho^m(\boldsymbol{x})\ddot{u}_i(\boldsymbol{x}, t) = 0, \tag{2a}$$

$$-\frac{D}{Dx_i} q_i(\boldsymbol{x}, t) + \tilde{r}(\boldsymbol{x}, t) - T_0 \frac{\partial}{\partial t} \int_{-\infty}^{t} \Big(\psi^m_{ij}(\boldsymbol{x}, t-\tau) \frac{D}{Dx_j} \dot{u}_i(\boldsymbol{x}, \tau) + \tilde{m}^m(\boldsymbol{x}, t-\tau)\dot{\theta}(\boldsymbol{x}, \tau) \Big) d\tau = 0, \tag{2b}$$

where there are the body forces $\boldsymbol{b}(\boldsymbol{x}, t) = b_i(\boldsymbol{x}, t)\mathbf{e}_i$, the material density $\rho^m(\boldsymbol{x})$, the displacement $\boldsymbol{u}(\boldsymbol{x}, t) = u_i(\boldsymbol{x}, t)\mathbf{e}_i$, the heat sources $\tilde{r}(\boldsymbol{x}, t) = r(\boldsymbol{x}, t)\, T_0$ and the relaxation form of constant $\tilde{m}^m(\boldsymbol{x}, t) = m^m(\boldsymbol{x}, t)\, T_0$ referred to the specific heat at constant strain. Over the cluster of cells $\mathcal{C} = [0, L] \times [0, \delta L]$, the body forces and the heat sources are supposed to be $\mathcal{C}$-periodic and to have vanishing mean values. Due to the $\mathcal{P}$-periodicity of the material, the tensors in equations (1a)-(2b) fulfill the rule $h^m(\boldsymbol{x} + \mathbf{v}_j, t) = h^m(\boldsymbol{x}, t), j = 1, 2, \forall \boldsymbol{x} \in \mathcal{P}$. Manipulating the balance and the constitutive equations (1a)-(2b) leads to the equations in the time domain

$$\frac{D}{Dx_j}\Big(\int_{-\infty}^{t} \Big(G^m_{ijhk}(\boldsymbol{x}, t-\tau)\dot{\varepsilon}_{hk}(\boldsymbol{x}, \tau) - \psi^m_{ij}(\boldsymbol{x}, t-\tau)\dot{\theta}(\boldsymbol{x}, \tau) \Big) d\tau \Big) + b_i(\boldsymbol{x}, t) - \rho^m(\boldsymbol{x})\ddot{u}_i(\boldsymbol{x}, t) = 0, \tag{3a}$$

$$\frac{D}{Dx_i}\Big(\int_{-\infty}^{t}\tilde{V}_{ij}^{m}(\boldsymbol{x},t-\tau)\frac{D}{Dx_j}\dot{\theta}(\boldsymbol{x},\tau)d\tau\Big)+\tilde{r}(\boldsymbol{x},t)+$$
$$-T_0\frac{\partial}{\partial t}\int_{-\infty}^{t}\Big(\psi_{ij}^{m}(\boldsymbol{x},t-\tau)\frac{D}{Dx_j}\dot{u}_i(\boldsymbol{x},\tau)+\tilde{m}^{m}(\boldsymbol{x},t-\tau)\dot{\theta}(\boldsymbol{x},\tau)\Big)d\tau=0. \tag{3b}$$

The periodic cell $\mathcal{P}$ can be rescaled with respect to the characteristic length ϵ by determining the nondimensional unit cell $\mathcal{U}=[0,1]\times[0,\delta]$ and giving rise to scales separation with the introduction of the macroscopic $\boldsymbol{x}\in\mathcal{P}$ and the microscopic $\boldsymbol{\xi}=\frac{\boldsymbol{x}}{\epsilon}\in\mathcal{U}$ variables. Therefore, the conditions concerning the tensors may be rewritten as $h^m(\boldsymbol{x},t)=h^m(\boldsymbol{\xi}=\frac{\boldsymbol{x}}{\epsilon},t)$. The two-sided Laplace transform of a generic function $h(\boldsymbol{x},t)$, which has been introduced as $\mathcal{L}(h(\boldsymbol{x},t)):=\hat{h}(\boldsymbol{x},s)$, $s\in\mathbb{C}$, allows recasting the equations (3a)-(3b) in the complex frequency domain as

$$\frac{D}{Dx_j}\Big(\hat{C}_{ijhk}^{m}\frac{D\hat{u}_h}{Dx_k}-\hat{\alpha}_{ij}^{m}\hat{\theta}\Big)+\hat{b}_i-\rho^m s^2\hat{u}_i=0, \tag{4a}$$

$$\frac{D}{Dx_i}\Big(\hat{K}_{ij}^{m}\frac{D\hat{\theta}}{Dx_j}\Big)-s\hat{\alpha}_{ij}^{m}\frac{D\hat{u}_i}{Dx_j}+\hat{r}-s\hat{p}^m\hat{\theta}=0, \tag{4b}$$

which are structurally analogous to the ones of the non-standard thermoelastic model presented in [34]. The transformed tensor components are defined as $\hat{C}_{ijhk}^{m}=s\hat{G}_{ijhk}^{m}$, $\hat{\alpha}_{ij}^{m}=s\hat{\psi}_{ij}^{m}$, $\hat{K}_{ij}^{m}=s\hat{V}_{ij}^{m}$, $\hat{p}^m=s\hat{m}^m$.
Based on this framework, to recast equations (4a)-(4b) into a novel formulation, the vector of unknowns $\hat{\boldsymbol{z}}(\boldsymbol{x},s)$ and the vector of source terms $\hat{\boldsymbol{g}}(\boldsymbol{x},s)$ are introduced as $\hat{\boldsymbol{z}}(\boldsymbol{x},s)=(\hat{\boldsymbol{u}}(\boldsymbol{x},s)\quad\hat{\theta}(\boldsymbol{x},s))^T$ and $\hat{\boldsymbol{g}}(\boldsymbol{x},s)=(\hat{\boldsymbol{b}}(\boldsymbol{x},s)\quad\hat{r}(\boldsymbol{x},s))^T$, respectively. Therefore, the equations (4a)-(4b) can be rewritten as

$$\frac{D}{Dx_j}\Big(\boldsymbol{A}_{jk}^{(1,0)}\frac{D\hat{\boldsymbol{z}}}{Dx_k}+\boldsymbol{A}_{j}^{(0,0)}\hat{\boldsymbol{z}}\Big)+s^2\boldsymbol{A}^{(0,2)}\hat{\boldsymbol{z}}+s(\boldsymbol{A}^{(0,1)}\hat{\boldsymbol{z}}+\boldsymbol{A}_{j}^{(1,1)}\frac{D\hat{\boldsymbol{z}}}{Dx_j})+\hat{\boldsymbol{g}}=\boldsymbol{0}, \tag{5}$$

where the square algebraic operators are defined as $\boldsymbol{A}_{jk}^{(1,0)}=A_{\alpha\beta}^{(1,0;jk)}\boldsymbol{e}_{\alpha\beta}$, $\boldsymbol{A}_{j}^{(0,0)}=A_{\alpha\beta}^{(0,0;j)}\boldsymbol{e}_{\alpha\beta}$, $\boldsymbol{A}^{(0,2)}=A_{\alpha\beta}^{(0,2)}\boldsymbol{e}_{\alpha\beta}$, $\boldsymbol{A}^{(0,1)}=A_{\alpha\beta}^{(0,1)}\boldsymbol{e}_{\alpha\beta}$, $\boldsymbol{A}_{j}^{(1,1)}=A_{\alpha\beta}^{(1,1;j)}\boldsymbol{e}_{\alpha\beta}$, with indices α and β varying according to the dimensionality of each operator and $j,k=1,2$. It should be noted that, in (5), the first superscript specifies the order of differentiation with respect to the spatial variable, while the second superscript indicates the corresponding power of s. Moreover, the square algebraic operators are $\mathcal{P}$-periodic and collect the components of the constitutive and inertial tensors involved in equations (4a)-(4b). The analysis of wave propagation in a periodic thermo-viscoelastic material can be addressed by applying the multidimensional Floquet-Bloch transform $\mathcal{F}_B$ to the field equations (4a)-(4b). For the unknown vector, $\hat{\boldsymbol{z}}(\boldsymbol{x},s)$, the transform is defined as $\mathcal{F}_B[\hat{\boldsymbol{z}}(\boldsymbol{x},s)]=\mathring{\boldsymbol{z}}(\boldsymbol{x},\boldsymbol{k},s)$, $\boldsymbol{k}\in\mathbb{C}$ (see [46] for technical details). Leveraging the $\mathcal{P}$-periodicity of the constitutive and inertial tensors and exploiting the Floquet-Bloch transform, equation (5) is cast in the wavevector domain as

$$\frac{D}{Dx_j}\Big(\boldsymbol{A}_{jk}^{(1,0)}\frac{D\mathring{\boldsymbol{z}}}{Dx_k}\Big)+\iota k_j\Big[(\boldsymbol{A}_{jk}^{(1,0)}+\boldsymbol{A}_{kj}^{(1,0)})\frac{D\mathring{\boldsymbol{z}}}{Dx_k}+(\boldsymbol{A}_{j}^{(0,0)}+s\boldsymbol{A}_{j}^{(1,1)}+\frac{D}{Dx_k}\boldsymbol{A}_{kj}^{(1,0)})\mathring{\boldsymbol{z}}\Big]+ \tag{6}$$
$$-(\boldsymbol{A}_{jk}^{(1,0)}k_jk_k-s^2\boldsymbol{A}^{(0,2)}-s\boldsymbol{A}^{(0,1)})\mathring{\boldsymbol{z}}+\Big(\boldsymbol{A}_{j}^{(0,0)}+s\boldsymbol{A}_{j}^{(1,1)}\Big)\frac{D\mathring{\boldsymbol{z}}}{Dx_j}+\mathring{\boldsymbol{g}}=\boldsymbol{0}.$$

In the case of free wave propagation $\mathring{\boldsymbol{g}}=\boldsymbol{0}$, the solution provides the dispersion spectrum of damped Bloch waves in terms of the complex frequency s parameterized on $\boldsymbol{k}\in\mathbb{R}^2$, namely with respect to the complex wave vector $\boldsymbol{k}$ parametrized on angular frequency $\omega\in\mathbb{R}$ and the polarization wave vectors. In the forced case $\mathring{\boldsymbol{g}}\neq\boldsymbol{0}$, it is possible to determine the forced response in the transformed Floquet-Bloch space and in the Laplace domain by solving the equation (6), then the solution could be retrieved in the physical space and in the time domain by using the inverse Fourier-Bloch and the Laplace transforms as

$$\mathcal{L}^{-1}[\mathcal{F}_B^{-1}[\mathring{\boldsymbol{z}}(\boldsymbol{x},\boldsymbol{k},s)]]=\boldsymbol{z}(\boldsymbol{x},t). \tag{7}$$

3 Multiscale modeling via asymptotic and variational-asymptotic homogenization schemes

This section outlines the main steps of the dynamic asymptotic homogenization approach. It introduces the asymptotic expansion of the microfields, displays the associated cell problems, and establishes the infinite

order average field equations. Finally, the identification of a first-order thermo-viscoelastic continuum is derived through a variational–asymptotic scheme. It should be observed that the applicability of the present homogenization approach relies on the assumption of a scale separation between the microstructural length of the periodic unit cell and the structural (or macroscopic) length. This fundamental condition guarantees the consistency of the multiscale expansion and the convergence of the deriving model.

3.1 Two-scale asymptotic homogenization scheme

This section outlines the asymptotic expansion of the vector, encompassing the transformed displacement and the transformed temperature, which is expressed with respect to the characteristic size. Moreover, the recursive differential problems, the cell problems, the down-scaling and the infinite-order average field equations are exposed. Specifically, the asymptotic expansion of the vector $\hat{\boldsymbol{z}}$ is recast in terms of the parameter ϵ as

$$\hat{\boldsymbol{z}}\Big(\boldsymbol{x}, \frac{\boldsymbol{x}}{\epsilon}, s\Big) = \sum_{l\in\mathbb{N}} \epsilon^l \hat{\boldsymbol{z}}^{(l)}\Big(\boldsymbol{x}, \frac{\boldsymbol{x}}{\epsilon}, s\Big). \tag{8}$$

Evoking the generalized total derivative of the function $\hat{\boldsymbol{z}}\Big(\boldsymbol{x}, \boldsymbol{\xi} = \frac{\boldsymbol{x}}{\epsilon}\Big)$ with respect to the variable x_k as

$$\frac{D}{Dx_k}\hat{\boldsymbol{z}}\Big(\boldsymbol{x}, \frac{\boldsymbol{x}}{\epsilon}\Big) = \Big(\frac{\partial \hat{\boldsymbol{z}}}{\partial x_k} + \frac{1}{\epsilon}\hat{\boldsymbol{z}}_{,k}\Big)\Big|_{\boldsymbol{\xi}=\frac{\boldsymbol{x}}{\epsilon}}, \tag{9}$$

the asymptotic expansion (8) is replaced into the equation (5) yielding the perturbative development of the field equation as

$$\begin{aligned}
&\epsilon^{-2}(\boldsymbol{A}^{(1,0)}_{jk}\hat{\boldsymbol{z}}^{(0)}_{,k})_{,j} + \epsilon^{-1}\Big[\Big(\boldsymbol{A}^{(1,0)}_{jk}\Big(\frac{\partial \hat{\boldsymbol{z}}^{(0)}}{\partial x_k} + \hat{\boldsymbol{z}}^{(1)}_{,k}\Big)\Big)_{,j} + \frac{\partial}{\partial x_j}(\boldsymbol{A}^{(1,0)}_{jk}\hat{\boldsymbol{z}}^{(0)}_{,k}) + (\boldsymbol{A}^{(0,0)}_{j}\hat{\boldsymbol{z}}^{(0)})_{,j} + s\boldsymbol{A}^{(1,1)}_{j}\hat{\boldsymbol{z}}^{(0)}_{,j}\Big] + \\
&+ \Big[\Big(\boldsymbol{A}^{(1,0)}_{jk}\Big(\frac{\partial \hat{\boldsymbol{z}}^{(1)}}{\partial x_k} + \hat{\boldsymbol{z}}^{(2)}_{,k}\Big)\Big)_{,j} + \frac{\partial}{\partial x_j}\Big(\boldsymbol{A}^{(1,0)}_{jk}\Big(\frac{\partial \hat{\boldsymbol{z}}^{(0)}}{\partial x_k} + \hat{\boldsymbol{z}}^{(1)}_{,k}\Big)\Big) + (\boldsymbol{A}^{(0,0)}_{j}\hat{\boldsymbol{z}}^{(1)})_{,j} + \frac{\partial}{\partial x_j}(\boldsymbol{A}^{(0,0)}_{j}\hat{\boldsymbol{z}}^{(0)}) + \\
&+ s\boldsymbol{A}^{(0,1)}\hat{\boldsymbol{z}}^{(0)} + s^2\boldsymbol{A}^{(0,2)}\hat{\boldsymbol{z}}^{(0)} + s\boldsymbol{A}^{(1,1)}_{j}\Big(\frac{\partial \hat{\boldsymbol{z}}^{(0)}}{\partial x_j} + \hat{\boldsymbol{z}}^{(1)}_{,j}\Big) + \hat{\boldsymbol{g}}\Big] + \\
&+ \epsilon\Big[\Big(\boldsymbol{A}^{(1,0)}_{jk}\Big(\frac{\partial \hat{\boldsymbol{z}}^{(2)}}{\partial x_k} + \hat{\boldsymbol{z}}^{(3)}_{,k}\Big)\Big)_{,j} + \frac{\partial}{\partial x_j}\Big(\boldsymbol{A}^{(1,0)}_{jk}\Big(\frac{\partial \hat{\boldsymbol{z}}^{(1)}}{\partial x_k} + \hat{\boldsymbol{z}}^{(2)}_{,k}\Big)\Big) + (\boldsymbol{A}^{(0,0)}_{j}\hat{\boldsymbol{z}}^{(2)})_{,j} + \frac{\partial}{\partial x_j}(\boldsymbol{A}^{(0,0)}_{j}\hat{\boldsymbol{z}}^{(1)}) + \\
&+ s\boldsymbol{A}^{(0,1)}\hat{\boldsymbol{z}}^{(1)} + s^2\boldsymbol{A}^{(0,2)}\hat{\boldsymbol{z}}^{(1)} + s\boldsymbol{A}^{(1,1)}_{j}\Big(\frac{\partial \hat{\boldsymbol{z}}^{(1)}}{\partial x_j} + \hat{\boldsymbol{z}}^{(2)}_{,j}\Big)\Big] + O(\epsilon^2) = \boldsymbol{0},
\end{aligned} \tag{10}$$

which can be rephrased in a compact way as

$$\epsilon^{-2}\boldsymbol{f}^{(0)}(\boldsymbol{x}, s) + \epsilon^{-1}\boldsymbol{f}^{(1)}(\boldsymbol{x}, s) + \boldsymbol{f}^{(2)}(\boldsymbol{x}, s) + ... + \epsilon^l \boldsymbol{f}^{(l+2)}(\boldsymbol{x}, s) + \hat{\boldsymbol{g}}(\boldsymbol{x}, s) = \boldsymbol{0}, \tag{11}$$

where $\boldsymbol{f}^{(i)}(\boldsymbol{x}, s)$ represent the source terms related to the mechanical and thermal differential problems for various orders of ϵ, they are independent of the fast variable $\boldsymbol{\xi}$ and, based on the equation perturbatively developed, they are derived as the mean value over the cell. Such terms can be determined at various order of ϵ. Indeed, for ϵ^{-2}, the differential problem, which derives from equation (10), is

$$(\boldsymbol{A}^{(1,0)}_{jk}\hat{\boldsymbol{z}}^{(0)}_{,k})_{,j} = \boldsymbol{f}^{(0)}(\boldsymbol{x}, s). \tag{12}$$

Introducing the vector of the transformed displacement and temperature at the macroscale as $\hat{\boldsymbol{Z}}(\boldsymbol{x}, s) = (\hat{\boldsymbol{U}}(\boldsymbol{x}, s) \quad \hat{\Theta}(\boldsymbol{x}, s))^T$, the solvability condition of problem (12) in the class of the $\mathcal{U}$-periodic functions enables to obtain the solution

$$\hat{\boldsymbol{z}}^{(0)}(\boldsymbol{x}, \boldsymbol{\xi}, s) = \hat{\boldsymbol{Z}}(\boldsymbol{x}, s), \tag{13}$$

which is affected by the macroscopic variable. The function (13) permits to determine the problem at the order ϵ^{-1} that is written as

$$(\boldsymbol{A}^{(1,0)}_{jk}\boldsymbol{z}^{(1)}_{,k})_{,j} + \boldsymbol{A}^{(1,0)}_{jk,j}\frac{\partial \hat{\boldsymbol{Z}}}{\partial x_k} + \boldsymbol{A}^{(0,0)}_{,j}\hat{\boldsymbol{Z}} = \boldsymbol{f}^{(1)}(\boldsymbol{x}, s), \tag{14}$$

whose solution is

$$\hat{\boldsymbol{z}}^{(1)}(\boldsymbol{x},\boldsymbol{\xi},s)=\boldsymbol{B}_{q_1}^{(1,1,0)}(\boldsymbol{\xi},s)\frac{\partial\hat{\boldsymbol{Z}}(\boldsymbol{x},s)}{\partial x_{q_1}}+\boldsymbol{B}^{(1,0,0)}(\boldsymbol{\xi},s)\hat{\boldsymbol{Z}}(\boldsymbol{x},s). \tag{15}$$

The square algebraic operators $\boldsymbol{B}_{q_1}^{(1,1,0)}=B_{\alpha\beta}^{(1,1,0;q_1)}\boldsymbol{e}_{\alpha\beta}$ and $\boldsymbol{B}^{(1,0,0)}=B_{\alpha\beta}^{(1,0,0)}\boldsymbol{e}_{\alpha\beta}$ collect the perturbation functions at the first-order, which are affected by the microscopic variable $\boldsymbol{\xi}$ and the Laplace variable s, whereas the first apex represents the order of the perturbative development. In the following, for the sake of simplicity and synthesis, the dependence on the variables is cancelled. Similarly, the solutions (13)-(15) permit to obtain the differential problem at the order ϵ^0 as

$$\begin{aligned}&(\boldsymbol{A}_{jk}^{(1,0)}\hat{\boldsymbol{z}}_{,k}^{(2)})_{,j}+\Big[(\boldsymbol{A}_{jq_2}^{(1,0)}\boldsymbol{B}_{q_1}^{(1,1,0)})_{,j}+\boldsymbol{A}_{q_1q_2}^{(1,0)}+\boldsymbol{A}_{q_2j}^{(1,0)}\boldsymbol{B}_{q_1,j}^{(1,1,0)}\Big]\frac{\partial^2\hat{\boldsymbol{Z}}}{\partial x_{q_1}\partial x_{q_2}}+\\&+\Big[(\boldsymbol{A}_{jq_1}^{(1,0)}\boldsymbol{B}^{(1,0,0)})_{,j}+\boldsymbol{A}_{q_1j}^{(1,0)}\boldsymbol{B}_{,j}^{(1,0,0)}+(\boldsymbol{A}_{j}^{(0,0)}\boldsymbol{B}_{q_1}^{(1,1,0)})_{,j}+\boldsymbol{A}_{q_1}^{(0,0)}\Big]\frac{\partial\hat{\boldsymbol{Z}}}{\partial x_{q_1}}+\\&+s^2\boldsymbol{A}^{(0,2)}\hat{\boldsymbol{Z}}+s\Big[\boldsymbol{A}_{j}^{(1,1)}\boldsymbol{B}_{q_1,j}^{(1,1,0)}+\boldsymbol{A}_{q_1}^{(1,1)}\Big]\frac{\partial\hat{\boldsymbol{Z}}}{\partial x_{q_1}}+s\Big[\boldsymbol{A}_{j}^{(1,1)}\boldsymbol{B}_{j}^{(1,0,0)}+\boldsymbol{A}^{(0,1)}\Big]\hat{\boldsymbol{Z}}=\boldsymbol{f}^{(2)}(\boldsymbol{x},s),\end{aligned} \tag{16}$$

whose solution is

$$\hat{\boldsymbol{z}}^{(2)}=\boldsymbol{B}_{q_1q_2}^{(2,2,0)}\frac{\partial^2\hat{\boldsymbol{Z}}(\boldsymbol{x},s)}{\partial x_{q_1}\partial x_{q_2}}+\boldsymbol{B}_{q_1}^{(2,1,0)}\frac{\partial\hat{\boldsymbol{Z}}(\boldsymbol{x},s)}{\partial x_{q_1}}+s\boldsymbol{B}^{(2,0,1)}\hat{\boldsymbol{Z}}(\boldsymbol{x},s)+s\boldsymbol{B}_{q_1}^{(2,1,1)}\frac{\partial\hat{\boldsymbol{Z}}(\boldsymbol{x},s)}{\partial x_{q_1}}+s^2\boldsymbol{B}^{(2,0,2)}\hat{\boldsymbol{Z}}(\boldsymbol{x},s), \tag{17}$$

where the square algebraic operators are defined as $\boldsymbol{B}_{q_1q_2}^{(2,2,0)}=B_{\alpha\beta}^{(2,2,0;q_1q_2)}\boldsymbol{e}_{\alpha\beta}$, $\boldsymbol{B}_{q_1}^{(2,1,0)}=B_{\alpha\beta}^{(2,1,0;q_1)}\boldsymbol{e}_{\alpha\beta}$, $\boldsymbol{B}^{(2,0,1)}=B_{\alpha\beta}^{(2,0,1)}\boldsymbol{e}_{\alpha\beta}$, $\boldsymbol{B}_{q_1}^{(2,1,1)}=B_{\alpha\beta}^{(2,1,1;q_1)}\boldsymbol{e}_{\alpha\beta}$ and $\boldsymbol{B}^{(2,0,2)}=B_{\alpha\beta}^{(2,0,2)}\boldsymbol{e}_{\alpha\beta}$ gather the perturbation functions at the second-order. After determining the solutions $\hat{\boldsymbol{z}}^{(0)}$, $\hat{\boldsymbol{z}}^{(1)}$ and $\hat{\boldsymbol{z}}^{(2)}$, it is worth achieving the cell problems. Indeed, replacing the solutions (13)-(15) into the recursive differential problem at the order ϵ^{-1}, (14), allows to derive the cell problems as

$$(\boldsymbol{A}_{jk}^{(1,0)}\boldsymbol{B}_{q_1,k}^{(1,1,0)})_{,j}+\boldsymbol{A}_{jq_1,j}^{(1,0)}=\boldsymbol{0},\qquad(\boldsymbol{A}_{jk}^{(1,0)}\boldsymbol{B}_{,k}^{(1,0,0)})_{,j}+\boldsymbol{A}_{j,j}^{(0,0)}=\boldsymbol{0}. \tag{18}$$

Moreover, the substitituion of the solutions (15)-(17) into the recursive differential problem at the order ϵ^0, (16), enables to derive the following cell problems

$$(\boldsymbol{A}_{jk}^{(1,0)}\boldsymbol{B}_{q_1q_2,k}^{(2,2,0)})_{,j}+(\boldsymbol{A}_{jq_2}^{(1,0)}\boldsymbol{B}_{q_1}^{(1,1,0)})_{,j}+\boldsymbol{A}_{q_1q_2}^{(1,0)}+\boldsymbol{A}_{q_2j}^{(1,0)}\boldsymbol{B}_{q_1,j}^{(1,1,0)}=\langle\boldsymbol{A}_{q_1q_2}^{(1,0)}+\boldsymbol{A}_{q_2j}^{(1,0)}\boldsymbol{B}_{q_1,j}^{(1,1,0)}\rangle, \tag{19a}$$

$$\begin{aligned}&(\boldsymbol{A}_{jk}^{(1,0)}\boldsymbol{B}_{q_1,k}^{(2,1,0)})_{,j}+(\boldsymbol{A}_{jq_1}^{(1,0)}\boldsymbol{B}^{(1,0,0)})_{,j}+\boldsymbol{A}_{q_1j}^{(1,0)}\boldsymbol{B}_{,j}^{(1,0,0)}+(\boldsymbol{A}_{j}^{(0,0)}\boldsymbol{B}_{q_1}^{(1,1,0)})_{,j}+\boldsymbol{A}_{q_1}^{(0,0)}=\\&=\langle\boldsymbol{A}_{q_1j}^{(1,0)}\boldsymbol{B}_{,j}^{(1,0,0)}+\boldsymbol{A}_{q_1}^{(0,0)}\rangle,\end{aligned} \tag{19b}$$

$$(\boldsymbol{A}_{jk}^{(1,0)}\boldsymbol{B}_{,k}^{(2,0,2)})_{,j}+\boldsymbol{A}^{(0,2)}=\langle\boldsymbol{A}^{(0,2)}\rangle, \tag{19c}$$

$$(\boldsymbol{A}_{jk}^{(1,0)}\boldsymbol{B}_{,k}^{(2,0,1)})_{,j}+\boldsymbol{A}_{j}^{(1,1)}\boldsymbol{B}_{j}^{(1,0,0)}+\boldsymbol{A}^{(0,1)}=\langle\boldsymbol{A}_{j}^{(1,1)}\boldsymbol{B}_{j}^{(1,0,0)}+\boldsymbol{A}^{(0,1)}\rangle, \tag{19d}$$

$$(\boldsymbol{A}_{jk}^{(1,0)}\boldsymbol{B}_{q_1,k}^{(2,1,1)})_{,j}+\boldsymbol{A}_{j}^{(1,1)}\boldsymbol{B}_{q_1,j}^{(1)}+\boldsymbol{A}_{q_1}^{(1,1)}=\langle\boldsymbol{A}_{j}^{(1,1)}\boldsymbol{B}_{q_1,j}^{(1)}+\boldsymbol{A}_{q_1}^{(1,1)}\rangle. \tag{19e}$$

It must be emphasized that the cell problems (18)-(19) are matrix partial differential equations. Referring to the solutions at different orders of ϵ that are (13), (15), (17), the down-scaling relation can be written as

$$\begin{aligned}\hat{\boldsymbol{z}}\Big(\boldsymbol{x},\frac{\boldsymbol{x}}{\epsilon},s\Big)=&\hat{\boldsymbol{Z}}(\boldsymbol{x},s)+\epsilon\Big(\boldsymbol{B}_{q_1}^{(1,1,0)}\frac{\partial\hat{\boldsymbol{Z}}(\boldsymbol{x},s)}{\partial x_{q_1}}+\boldsymbol{B}^{(1,0,0)}\hat{\boldsymbol{Z}}(\boldsymbol{x},s)\Big)+\epsilon^2\Big(\boldsymbol{B}_{q_1q_2}^{(2,2,0)}\frac{\partial^2\hat{\boldsymbol{Z}}(\boldsymbol{x},s)}{\partial x_{q_1}\partial x_{q_2}}+\\&+\boldsymbol{B}_{q_1}^{(2,1,0)}\frac{\partial\hat{\boldsymbol{Z}}(\boldsymbol{x},s)}{\partial x_{q_1}}+s\boldsymbol{B}^{(2,0,1)}\hat{\boldsymbol{Z}}(\boldsymbol{x},s)+s\boldsymbol{B}_{q_1}^{(2,1,1)}\frac{\partial\hat{\boldsymbol{Z}}(\boldsymbol{x},s)}{\partial x_{q_1}}+s^2\boldsymbol{B}^{(2,0,2)}\hat{\boldsymbol{Z}}(\boldsymbol{x},s)\Big)+O(\epsilon^3)\Big\}\Big|_{\boldsymbol{\xi}=\frac{\boldsymbol{x}}{\epsilon}}.\end{aligned} \tag{20}$$

Moreover, the up-scaling relation enables to express the transformed macro-fields as the average on the translation of the transformed micro-fields as

$$\hat{\boldsymbol{Z}}(\boldsymbol{x},s)=\Big\langle\hat{\boldsymbol{z}}\Big(\boldsymbol{x},\frac{\boldsymbol{x}}{\epsilon}+\boldsymbol{\zeta},s\Big)\Big\rangle, \tag{21}$$

where $\boldsymbol{\zeta} \in \mathcal{U}$ is the translation variable with $\epsilon\boldsymbol{\zeta} \in \mathcal{P}$, which determines the translation of the heterogeneous domain with respect to $\mathcal{C}$-periodic source terms. The average field equation of infinite order follows from the substitution of the down-scaling relation (20) into the equation at the microscale (5) as

$$\begin{aligned}
&\boldsymbol{n}^{(2,2,0)}_{q_1q_2}\frac{\partial^2\hat{\boldsymbol{Z}}}{\partial x_{q_1}\partial x_{q_2}}+\boldsymbol{n}^{(2,0,2)}s^2\hat{\boldsymbol{Z}}+\boldsymbol{n}^{(2,1,0)}_{q_1}\frac{\partial\hat{\boldsymbol{Z}}}{\partial x_{q_1}}+s\boldsymbol{n}^{(2,1,1)}_{q_1}\frac{\partial\hat{\boldsymbol{Z}}}{\partial x_{q_1}}+s\boldsymbol{n}^{(2,0,1)}\hat{\boldsymbol{Z}}+\hat{\boldsymbol{g}}+\epsilon\Big(\boldsymbol{n}^{(3,3,0)}_{q_1q_2q_3}\frac{\partial^3\hat{\boldsymbol{Z}}}{\partial x_{q_1}\partial x_{q_2}\partial x_{q_3}}+\\
&+\boldsymbol{n}^{(3,2,0)}_{q_1q_2}\frac{\partial^2\hat{\boldsymbol{Z}}}{\partial x_{q_1}\partial x_{q_2}}+s^2\boldsymbol{n}^{(3,1,2)}_{q_1}\frac{\partial\hat{\boldsymbol{Z}}}{\partial x_{q_1}}+s^2\boldsymbol{n}^{(3,0,2)}\hat{\boldsymbol{Z}}+s\boldsymbol{n}^{(3,2,1)}_{q_1q_2}\frac{\partial^2\hat{\boldsymbol{Z}}}{\partial x_{q_1}\partial x_{q_2}}+s\boldsymbol{n}^{(3,1,1)}_{q_1}\frac{\partial\hat{\boldsymbol{Z}}}{\partial x_{q_1}}+s^3\boldsymbol{n}^{(3,0,3)}\hat{\boldsymbol{Z}}\Big)+\\
&+\epsilon^2\Big(\boldsymbol{n}^{(4,4,0)}_{q_1q_2q_3q_4}\frac{\partial^4\hat{\boldsymbol{Z}}}{\partial x_{q_1}\partial x_{q_2}\partial x_{q_3}\partial x_{q_4}}+\boldsymbol{n}^{(4,3,0)}_{q_1q_2q_3}\frac{\partial^3\hat{\boldsymbol{Z}}}{\partial x_{q_1}\partial x_{q_2}\partial x_{q_3}}+s^2\boldsymbol{n}^{(4,2,2)}_{q_1q_2}\frac{\partial^2\hat{\boldsymbol{Z}}}{\partial x_{q_1}\partial x_{q_2}}+s^2\boldsymbol{n}^{(4,1,2)}_{q_1}\frac{\partial\hat{\boldsymbol{Z}}}{\partial x_{q_1}}+\\
&+s\boldsymbol{n}^{(4,3,1)}_{q_1q_2q_3}\frac{\partial^3\hat{\boldsymbol{Z}}}{\partial x_{q_1}\partial x_{q_2}\partial x_{q_3}}+s\boldsymbol{n}^{(4,2,1)}_{q_1q_2}\frac{\partial^2\hat{\boldsymbol{Z}}}{\partial x_{q_1}\partial x_{q_2}}+s^3\boldsymbol{n}^{(4,1,3)}_{q_1}\frac{\partial\hat{\boldsymbol{Z}}}{\partial x_{q_1}}-\boldsymbol{n}^{(4,2,0)}_{q_1q_2}\frac{\partial^2\hat{\boldsymbol{Z}}}{\partial x_{q_1}\partial x_{q_2}}-s\boldsymbol{n}^{(4,1,1)}_{q_1}\frac{\partial\hat{\boldsymbol{Z}}}{\partial x_{q_1}}+\\
&-s^4\boldsymbol{n}^{(4,0,4)}\hat{\boldsymbol{Z}}-s^2\boldsymbol{n}^{(4,1,2)}_{q_1}\frac{\partial\hat{\boldsymbol{Z}}}{\partial x_{q_1}}-s^2\boldsymbol{n}^{(4,0,2)}\hat{\boldsymbol{Z}}-s^3\boldsymbol{n}^{(4,0,3)}\hat{\boldsymbol{Z}}\Big)+O(\epsilon^3)=\boldsymbol{0},
\end{aligned}\tag{22}$$

where the algebraic functions consist of the coefficients multiplying the gradients of the transformed macro-fields and represent the known terms of the cell problems. Moreover, the first superscript increases with the truncation order, the second indicates the order of the spatial differential operator, and the third corresponds to the power of s. Moreover, they can be expressed as the mean values over the unit cell $\mathcal{U}$ with respect to a linear combination of perturbation functions and transformed constitutive and inertial tensors at the microscale. In order to tackle with the average field equation of infinite order (22), some resolution strategies will be proposed in the next session. In case of free wave propagation, a proper truncation of (22) at even orders of the characteristic size will be performed to achieve the spectra at various approximation orders resulting in the algebraic problems with respect to $(\boldsymbol{k}, s)$ that govern the propagation. Concerning with the forced dynamic wave propagation, a perturbative technique will be performed based on the expansion in terms of ϵ of the vector collecting the transformed macro-fields. A further strategy to identify the field equations that govern higher-order materials are represented by the variational-asymptotic techniques, which will be highlighted in the Section (3.2) at the first order. Based on the definition of a functional, such variational-asymptotic schemes enable to achieve field equations for the equivalent homogeneous materials with respect to the overall constitutive and inertial tensors by enforcing the stationarity of the first variation of the functional and truncating it at a certain order of the microscopical length.

3.1.1 Free wave propagation

The free wave propagation in an unbounded thermo-viscoelastic periodic material is herein investigated by applying the Fourier transform to the macro-field vector $\hat{\boldsymbol{Z}}$ associated with equation (22), namely $\mathcal{F}[\hat{\boldsymbol{Z}}(\boldsymbol{x}, s)] = \check{\boldsymbol{Z}}(\boldsymbol{k}, s)$, which leads to

$$\begin{aligned}
&[(\iota^2\boldsymbol{n}^{(2,2,0)}_{q_1q_2}k_{q_1}k_{q_2}+s^2\boldsymbol{n}^{(2,0,2)}+\iota\boldsymbol{n}^{(2,1,0)}_{q_1}k_{q_1}+s\iota\boldsymbol{n}^{(2,1,1)}_{q_1}k_{q_1}+s\boldsymbol{n}^{(2,0,1)})+\\
&+\epsilon(\iota^3\boldsymbol{n}^{(3,3,0)}_{q_1q_2q_3}k_{q_1}k_{q_2}k_{q_3}+\iota^2\boldsymbol{n}^{(3,2,0)}_{q_1q_2}k_{q_1}k_{q_2}+s^2\iota\boldsymbol{n}^{(3,1,2)}_{q_1}k_{q_1}+s^2\boldsymbol{n}^{(3,0,2)}+s\iota^2\boldsymbol{n}^{(3,2,1)}_{q_1q_2}k_{q_1}k_{q_2}+s\iota\boldsymbol{n}^{(3,1,1)}_{q_1}k_{q_1}+\\
&+s^3\boldsymbol{n}^{(3,0,3)})+\epsilon^2(\iota^4\boldsymbol{n}^{(4,4,0)}_{q_1q_2q_3q_4}k_{q_1}k_{q_2}k_{q_3}k_{q_4}+\iota^3\boldsymbol{n}^{(4,3,0)}_{q_1q_2q_3}k_{q_1}k_{q_2}k_{q_3}+s^2\iota^2\boldsymbol{n}^{(4,2,2)}_{q_1q_2}k_{q_1}k_{q_2}+s^2\iota\boldsymbol{n}^{(4,1,2)}_{q_1}k_{q_1}+\\
&+s\iota^2\boldsymbol{n}^{(4,2,1)}_{q_1q_2}k_{q_1}k_{q_2}+s^3\iota\boldsymbol{n}^{(4,1,3)}_{q_1}k_{q_1}-\iota^2\boldsymbol{n}^{(4,2,0)}_{q_1q_2}k_{q_1}k_{q_2}-s\iota\boldsymbol{n}^{(4,1,1)}_{q_1}k_{q_1}-s^4\boldsymbol{n}^{(4,0,4)}-s^2\iota\boldsymbol{n}^{(4,1,2)}_{q_1}k_{q_1}+\\
&-s^2\boldsymbol{n}^{(4,0,2)}-s^3\boldsymbol{n}^{(4,0,3)}+s\iota^3\boldsymbol{n}^{(4,3,1)}_{q_1q_2q_3}k_{q_1}k_{q_2}k_{q_3})]\check{\boldsymbol{Z}}+O(\epsilon^3)=\boldsymbol{0},
\end{aligned}\tag{23}$$

in the frequency-wavevector domain. In the framework of free wave propagation, the equation (23) may be summarized by gathering the matrices according to increasing powers of ϵ as

$$(\boldsymbol{C}^{(0)}(\boldsymbol{k}, s)+\epsilon\boldsymbol{C}^{(1)}(\boldsymbol{k}, s)+\epsilon^2\boldsymbol{C}^{(2)}(\boldsymbol{k}, s)+O(\epsilon^3))\check{\boldsymbol{Z}}(\boldsymbol{k}, s)=\boldsymbol{0},\tag{24}$$

where the $(\boldsymbol{k}, s)$-dependent matrices $\boldsymbol{C}^{(0)}, \boldsymbol{C}^{(1)}$ and $\boldsymbol{C}^{(2)}$ that refer to the equation (24) are listed as

$$\boldsymbol{C}^{(0)}=\boldsymbol{n}^{(2,2,0)}_{q_1q_2}k_{q_1}k_{q_2}+s^2\boldsymbol{n}^{(2,0,2)}+\iota\boldsymbol{n}^{(2,1,0)}_{q_1}k_{q_1}+s\iota\boldsymbol{n}^{(2,1,1)}_{q_1}k_{q_1}+s\boldsymbol{n}^{(2,0,1)},\tag{25a}$$

$$\boldsymbol{C}^{(1)}=\iota\boldsymbol{n}^{(3,3,0)}_{q_1q_2q_3}k_{q_1}k_{q_2}k_{q_3}+\boldsymbol{n}^{(3,2,0)}_{q_1q_2}k_{q_1}k_{q_2}+s^2\iota\boldsymbol{n}^{(3,1,2)}_{q_1}k_{q_1}+s^2\boldsymbol{n}^{(3,0,2)}-s\boldsymbol{n}^{(3,2,1)}_{q_1q_2}k_{q_1}k_{q_2}+$$

$$+ s\iota \boldsymbol{n}^{(3,1,1)}_{q_1} k_{q_1} + s^3 \boldsymbol{n}^{(3,0,3)}, \tag{25b}$$

$$\begin{aligned}\boldsymbol{C}^{(2)} =& \boldsymbol{n}^{(4,4,0)}_{q_1q_2q_3q_4} k_{q_1}k_{q_2}k_{q_3}k_{q_4} + \iota \boldsymbol{n}^{(4,3,0)}_{q_1q_2q_3} k_{q_1}k_{q_2}k_{q_3} - s^2 \boldsymbol{n}^{(4,2,2)}_{q_1q_2} k_{q_1}k_{q_2} + s^2\iota \boldsymbol{n}^{(4,1,2)}_{q_1} k_{q_1} + \\ & - s \boldsymbol{n}^{(4,2,1)}_{q_1q_2} k_{q_1}k_{q_2} + s^3\iota \boldsymbol{n}^{(4,1,3)}_{q_1} k_{q_1} + \boldsymbol{n}^{(4,2,0)}_{q_1q_2} k_{q_1}k_{q_2} - s\iota \boldsymbol{n}^{(4,1,1)}_{q_1} k_{q_1} + s^4 \boldsymbol{n}^{(4,0,4)} - s^2\iota \boldsymbol{n}^{(4,1,2)}_{q_1} k_{q_1} + \\ & - s^2 \boldsymbol{n}^{(4,0,2)} + s^3 \boldsymbol{n}^{(4,0,3)} + s\iota^3 \boldsymbol{n}^{(4,3,1)}_{q_1q_2q_3} k_{q_1}k_{q_2}k_{q_3}.\end{aligned} \tag{25c}$$

In order to derive the dispersion properties of a thermo-viscoelastic periodic material when the source terms are set at zero, the equation (24) can be properly truncated at the zeroth order of ϵ resulting as

$$(\boldsymbol{C}^{(0)}(\boldsymbol{k}, s))\check{\boldsymbol{Z}}(\boldsymbol{k}, s) = \boldsymbol{0}. \tag{26}$$

In such a case, the complex spectrum of the material can be derived by solving the characteristic equation as

$$\mathcal{G}^0(\boldsymbol{k}, s) = \det\left(\boldsymbol{C}^{(0)}\right) = \boldsymbol{0}, \tag{27}$$

which rely on the complex-valued wavevector $\boldsymbol{k}$ and the complex-valued angular frequency s. It must be emphasized that solving the characteristic equation (27) provides an approximate complex spectrum of a visco-thermoelastic periodic material that is equivalent to the complex spectrum characterizing a first-order homogenized material. Moreover, a second-order approximation of the spectrum can be retrieved by truncating the equation (24) at the second order of ϵ yielding

$$\Big(\sum_{j=0}^{2} \epsilon^j \boldsymbol{C}^{(j)}(\boldsymbol{k}, s)\Big)\check{\boldsymbol{Z}}(\boldsymbol{k}, s) = \boldsymbol{0}, \tag{28}$$

and determining the roots of the characteristic equation as

$$\mathcal{G}^2(\boldsymbol{k}, s) = \det\Big(\sum_{j=0}^{2} \epsilon^j \boldsymbol{C}^{(j)}(\boldsymbol{k}, s)\Big) = \boldsymbol{0}. \tag{29}$$

Expressing the characteristic equations (27) and (29) as their real parts and imaginary parts $\mathcal{G}^j(\boldsymbol{k}, s) = \mathcal{R}e(\mathcal{G}^j(\boldsymbol{k}, s)) + \iota\mathcal{I}m(\mathcal{G}^j(\boldsymbol{k}, s))$, $j = 0, 2$, enables to alternatively derive the complex spectrum as the intersection of the hyper-surfaces

$$\begin{cases} \mathcal{R}e(\mathcal{G}^j(\mathcal{R}e(\boldsymbol{k}), \mathcal{I}m(\boldsymbol{k}), \mathcal{R}e(s), \mathcal{I}m(s))) = \boldsymbol{0} \\ \mathcal{I}m(\mathcal{G}^j(\mathcal{R}e(\boldsymbol{k}), \mathcal{I}m(\boldsymbol{k}), \mathcal{R}e(s), \mathcal{I}m(s))) = \boldsymbol{0} \end{cases}. \tag{30}$$

It must be remarked that the complex spectrum herein derived is a low-frequency approximation of the one retrieved by solving the equation (6) in the null source conditions.

3.1.2 Forced wave propagation

A perturbative scheme is described to formally solve the average field equations of infinite order (22) by carrying out an asymptotic expansion of the transformed macro-fields vector $\hat{\boldsymbol{Z}}$ with respect to the power of the microstructural size ϵ as

$$\hat{\boldsymbol{Z}} = \sum_{j\in\mathbb{N}} \epsilon^j \hat{\boldsymbol{Z}}^{(j)}. \tag{31}$$

Replacing the asymptotic expansion of the transformed macro-field vector (31) into the average field equation of infinite order (22) yields an expression that can be reorganized so that all contributions can be collected according to their power of the microstructural length scale ϵ as

$$\begin{aligned}& \boldsymbol{n}^{(2,2,0)}_{q_1q_2} \sum_{l\in\mathbb{N}} \epsilon^l \frac{\partial^2 \hat{\boldsymbol{Z}}^{(l)}}{\partial x_{q_1}\partial x_{q_2}} + \left(\sum_{\upsilon=0}^{1} s^\upsilon \boldsymbol{n}^{(2,1,\upsilon)}_{q_1}\right) \sum_{l\in\mathbb{N}} \epsilon^l \frac{\partial \hat{\boldsymbol{Z}}^{(l)}}{\partial x_{q_1}} + \left(\sum_{\upsilon=1}^{2} s^\upsilon \boldsymbol{n}^{(2,0,\upsilon)}\right) \sum_{l\in\mathbb{N}} \epsilon^l \hat{\boldsymbol{Z}}^{(l)} + \hat{\boldsymbol{g}} + \\ & + \epsilon \left[\boldsymbol{n}^{(3,3,0)}_{q_1q_2q_3} \sum_{l\in\mathbb{N}} \epsilon^l \frac{\partial^3 \hat{\boldsymbol{Z}}^{(l)}}{\partial x_{q_1}\partial x_{q_2}\partial x_{q_3}} + \left(\sum_{\upsilon=0}^{1} s^\upsilon \boldsymbol{n}^{(3,2,\upsilon)}_{q_1q_2}\right) \sum_{l\in\mathbb{N}} \epsilon^l \frac{\partial^2 \hat{\boldsymbol{Z}}^{(l)}}{\partial x_{q_1}\partial x_{q_2}} + \right.\end{aligned}$$

$$+\left(\sum_{\upsilon=1}^{2} s^{\upsilon}\boldsymbol{n}^{(3,1,\upsilon)}_{q_1}\right)\sum_{l\in\mathbb{N}}\epsilon^l\frac{\partial\hat{\boldsymbol{Z}}^{(l)}}{\partial x_{q_1}}+\left(\sum_{\upsilon=2}^{3} s^{\upsilon}\boldsymbol{n}^{(3,0,\upsilon)}\right)\sum_{l\in\mathbb{N}}\epsilon^l\hat{\boldsymbol{Z}}^{(l)}\Bigg]+$$
$$+\epsilon^2\Bigg[\left(\boldsymbol{n}^{(4,4,0)}_{q_1q_2q_3q_4}\right)\sum_{l\in\mathbb{N}}\epsilon^l\frac{\partial^4\hat{\boldsymbol{Z}}^{(l)}}{\partial x_{q_1}\partial x_{q_2}\partial x_{q_3}\partial x_{q_4}}+\left(\sum_{\upsilon=0}^{1} s^{\upsilon}\boldsymbol{n}^{(4,3,\upsilon)}_{q_1q_2q_3}\right)\sum_{l\in\mathbb{N}}\epsilon^l\frac{\partial^3\hat{\boldsymbol{Z}}^{(l)}}{\partial x_{q_1}\partial x_{q_2}\partial x_{q_3}}+$$
$$+\left(\sum_{\upsilon=0}^{2}(-1)^{\delta_{0\upsilon}}s^{\upsilon}\boldsymbol{n}^{(4,2,\upsilon)}_{q_1q_2}\right)\sum_{l\in\mathbb{N}}\epsilon^l\frac{\partial^2\hat{\boldsymbol{Z}}^{(l)}}{\partial x_{q_1}\partial x_{q_2}}+\left(\sum_{\upsilon=1}^{3}(-1)^{\delta_{1\upsilon}}s^{\upsilon}\boldsymbol{n}^{(4,1,\upsilon)}_{q_1}\right)\sum_{l\in\mathbb{N}}\epsilon^l\frac{\partial\hat{\boldsymbol{Z}}^{(l)}}{\partial x_{q_1}}+$$
$$-\left(\sum_{\upsilon=2}^{4} s^{\upsilon}\boldsymbol{n}^{(4,0,\upsilon)}\right)\sum_{l\in\mathbb{N}}\epsilon^l\hat{\boldsymbol{Z}}^{(l)}\Bigg]+\ldots=\boldsymbol{0}, \tag{32}$$

where $\delta_{i\upsilon}$ is the Kronecker delta. This procedure allows gathering terms of identical order, which generates a hierarchy of macroscopic recursive problems. At the order ϵ^0, one obtains the equation

$$\boldsymbol{n}^{(2,2,0)}_{q_1q_2}\frac{\partial^2\hat{\boldsymbol{Z}}^{(0)}}{\partial x_{q_1}\partial x_{q_2}}+\boldsymbol{n}^{(2,0,2)}s^2\hat{\boldsymbol{Z}}^{(0)}+\boldsymbol{n}^{(2,1,0)}_{q_1}\frac{\partial\hat{\boldsymbol{Z}}^{(0)}}{\partial x_{q_1}}+s\boldsymbol{n}^{(2,1,1)}_{q_1}\frac{\partial\hat{\boldsymbol{Z}}^{(0)}}{\partial x_{q_1}}+s\boldsymbol{n}^{(2,0,1)}\hat{\boldsymbol{Z}}^{(0)}+\hat{\boldsymbol{g}}=\boldsymbol{0}, \tag{33}$$

which exhibits the same mathematical structure as the equation governing a first-order visco-thermoelastic continuum. Higher-order approximations can be obtained by truncating the expansion at increasing orders of ϵ, yielding problems that are featured by the same structure as those characterizing the first-order continuum. For instance, at the orders ϵ^j, with $j=1,2$, one derives

$$\boldsymbol{n}^{(2,2,0)}_{q_1q_2}\frac{\partial^2\hat{\boldsymbol{Z}}^{(j)}}{\partial x_{q_1}\partial x_{q_2}}+\boldsymbol{n}^{(2,0,2)}s^2\hat{\boldsymbol{Z}}^{(j)}+\boldsymbol{n}^{(2,1,0)}_{q_1}\frac{\partial\hat{\boldsymbol{Z}}^{(j)}}{\partial x_{q_1}}+s\boldsymbol{n}^{(2,1,1)}_{q_1}\frac{\partial\hat{\boldsymbol{Z}}^{(j)}}{\partial x_{q_1}}+s\boldsymbol{n}^{(2,0,1)}\hat{\boldsymbol{Z}}^{(j)}+\hat{\boldsymbol{g}}^{(j-1)}=\boldsymbol{0}, \tag{34}$$

where $\hat{\boldsymbol{g}}^{(j-1)}$ denotes the known $\mathcal{C}$-periodic source terms, which contains the non-local contributions arising from the average field equations at the previous orders.
An alternative strategy to deal with the forced wave propagation problem is to truncate equation (22), appropriately, that is, for even orders of ϵ. After that, by transforming in the $\boldsymbol{k}$ space and in the transformed Laplace space this yields

$$\check{\boldsymbol{Z}}(\boldsymbol{k},s)=\Big(\sum_{j\in\mathbb{N}}\epsilon^{(2j)}\boldsymbol{C}^{(2j)}(\boldsymbol{k},s)\Big)^{-1}\check{\boldsymbol{g}}(\boldsymbol{k},s), \tag{35}$$

which can be retrieved in the physical space and in the time domain by using the definition (7).
It is important to remark that the approximation of the solution at the microscale can be determined through the down-scaling relation (20), which involves the perturbation functions characterizing the microstructure of the periodic material, as well as the solution at the macroscale and its associated macroscopic gradients.

3.2 First-order identification via asymptotic variational procedure

In this section, a variational-asymptotic scheme is described to obtain the field equations governing the equivalent homogeneous medium. Such a method is based on the definition of the power-like functional in the Laplace domain, $\mathcal{L}(\Lambda)$, that depends on the power-like density, $\hat{\lambda}_m$, and is defined over the periodic domain $\mathcal{C}$ in components as

$$\begin{aligned}\hat{\Lambda}=\mathcal{L}(\Lambda)&=\int_{\mathcal{C}}\hat{\lambda}_m\Big(\boldsymbol{x},\frac{\boldsymbol{x}}{\epsilon}\Big)d\boldsymbol{x}= \\ &=\int_{\mathcal{C}}s\Big(\frac{1}{2}s^2A^{(0,2)}_{\alpha\beta}\hat{z}_\alpha\hat{z}_\beta+\frac{1}{2}\frac{D\hat{z}_\alpha}{Dx_j}A^{(1,0;jk)}_{\alpha\beta}\frac{D\hat{z}_\beta}{Dx_k}-\frac{1}{2}\frac{D\hat{z}_\alpha}{Dx_j}A^{(0,0;j)}_{\alpha\beta}\hat{z}_\beta-\hat{z}_\alpha\hat{g}_\alpha\Big)+ \\ &-\frac{1}{2}s\Big(\frac{D\hat{z}_\alpha}{Dx_j}A^{(1,1;j)}_{\alpha\beta}\hat{z}_\beta+A^{(0,1)}_{\alpha\beta}\hat{z}_\alpha\hat{z}_\beta\Big)d\boldsymbol{x},\end{aligned} \tag{36}$$

where $j,k=1,2$ whereas α and β vary according to the operator's dimensionality. It is worth noticing that the transformed power-like functional $\hat{\Lambda}$ and the power-like density $\hat{\lambda}_m$ are affected by the translation

variable $\boldsymbol{\zeta} \in \mathcal{U}$, then the transformed tensors defined in (1a)-(2b) rely on the translation variable $\boldsymbol{\zeta}$ resulting in $\hat{h}^{m,\zeta}\Big(\boldsymbol{x}, \frac{\boldsymbol{x}}{\epsilon}\Big) = \hat{h}^{m}\Big(\boldsymbol{x}, \frac{\boldsymbol{x}}{\epsilon} + \boldsymbol{\zeta}\Big)$ and consequently the operators defined in (15)-(17), collecting the perturbation functions, depend upon the variable $\boldsymbol{\zeta}$. Furthermore, the power-like density in the Laplace domain, $\hat{\lambda}_m$, obeys the periodicity condition $\hat{\lambda}_m^{\zeta}\Big(\boldsymbol{x}, \frac{\boldsymbol{x}}{\epsilon}\Big) = \hat{\lambda}_m\Big(\boldsymbol{x}, \frac{\boldsymbol{x}}{\epsilon} + \boldsymbol{\zeta}\Big)$, so that the power-like functional in the Laplace domain, $\hat{\Lambda}$, can be rewritten as

$$\hat{\Lambda}^{\zeta} = \hat{\Lambda}(\boldsymbol{\zeta}) = \int_{\mathcal{C}} \hat{\lambda}_m^{\zeta}\Big(\boldsymbol{x}, \frac{\boldsymbol{x}}{\epsilon}\Big) d\boldsymbol{x} = \int_{\mathcal{C}} \hat{\lambda}_m\Big(\boldsymbol{x}, \frac{\boldsymbol{x}}{\epsilon} + \boldsymbol{\zeta}\Big) d\boldsymbol{x}. \tag{37}$$

Let $\hat{\Lambda}_m$ define the average transformed power-like functional at the microscale as

$$\hat{\Lambda}_m \doteq \langle \hat{\Lambda}^{\zeta} \rangle = \frac{1}{|\mathcal{U}|} \int_{\mathcal{U}} \hat{\Lambda}^{\zeta} d\boldsymbol{\zeta} = \frac{1}{|\mathcal{U}|} \int_{\mathcal{U}} \hat{\Lambda}(\boldsymbol{\zeta}) d\boldsymbol{\zeta} = \int_{\mathcal{C}} \Big\langle \hat{\lambda}_m\Big(\boldsymbol{x}, \frac{\boldsymbol{x}}{\epsilon} + \boldsymbol{\zeta}\Big) \Big\rangle d\boldsymbol{x}, \tag{38}$$

where the Fubini theorem is applied, and it is independent of the translation variable $\boldsymbol{\zeta}$, as $\hat{\Lambda}^{\zeta}$ is derived by taking the mean over the translated realizations of the microstructure, [19, 47]. Therefore, the transformed power-like density at the microscale fulfills the important condition

$$\Big\langle \hat{\lambda}_m\Big(\boldsymbol{x}, \frac{\boldsymbol{x}}{\epsilon} + \boldsymbol{\zeta}\Big) \Big\rangle = \frac{1}{|\mathcal{U}|} \int_{\mathcal{U}} \hat{\lambda}_m\Big(\boldsymbol{x}, \frac{\boldsymbol{x}}{\epsilon} + \boldsymbol{\zeta}\Big) d\boldsymbol{\zeta} = \frac{1}{|\mathcal{U}|} \int_{\mathcal{U}} \hat{\lambda}_m\Big(\boldsymbol{x}, \boldsymbol{\xi}\Big) d\boldsymbol{\xi} = \langle \hat{\lambda}_m(\boldsymbol{x}, \boldsymbol{\xi}) \rangle, \tag{39}$$

where $|\mathcal{U}|$ represents the size of the unitary cell. With the scope of recasting $\hat{\Lambda}_m$ in terms of transformed macro-fields, the total derivative of the transformed micro-fields is considered as

$$\begin{aligned} \frac{D\hat{z}_{\alpha}}{Dx_k} &= \frac{\partial \hat{Z}_{\alpha}}{\partial x_k} + \Big(B^{(1,1,0;q_1)}_{\alpha\beta,k} \frac{\partial \hat{Z}_{\beta}}{\partial x_{q_1}} + B^{(1,0,0)}_{\alpha\delta,k} \hat{Z}_{\delta}\Big) + \epsilon\Big(B^{(1,1,0;q_1)}_{\alpha\beta} \frac{\partial^2 \hat{Z}_{\beta}}{\partial x_{q_1} \partial x_k} + B^{(1,0,0)}_{\alpha\delta} \frac{\partial \hat{Z}_{\delta}}{\partial x_k}\Big) + O(\epsilon^2) = \\ &= (\delta_{kq_1}\delta_{\alpha\beta} + B^{(1,1,0;q_1)}_{\alpha\beta,k}) \frac{\partial \hat{Z}_{\alpha}}{\partial x_{q_1}} + B^{(1,0,0)}_{\alpha\delta,k} \hat{Z}_{\delta} + O(\epsilon) = P^{(1,1,0;kq_1)}_{\alpha\beta} \frac{\partial \hat{Z}_{\alpha}}{\partial x_{q_1}} + P^{(1,0,0;k)}_{\alpha\delta} \hat{Z}_{\delta} + O(\epsilon), \end{aligned} \tag{40}$$

where $P^{(1,1,0;kq_1)}_{\alpha\beta}$ and $P^{(1,0,0;k)}_{\alpha\delta}$ are the linear operator components related to the first-order perturbation functions, which are $\mathcal{U}$-periodic. Leveraging on the mentioned linear operators, it is possible to introduce the following operators that can be written in components as

$$\begin{aligned} m^{(2,0)}_{\alpha\beta} &= \langle P^{(1,1,0;jr_1)}_{\alpha\gamma} A^{(1,0;jk)}_{\alpha\beta} P^{(1,1,0;kq_1)}_{\beta\zeta} \rangle, \\ m^{(0,2)}_{\alpha\beta} &= \langle A^{(0,2)}_{\alpha\beta} \rangle, \\ m^{(1,0)}_{\alpha\beta} &= \langle P^{(1,1,0;jq_1)}_{\alpha\gamma} A^{(0,0;j)}_{\alpha\beta} - P^{(1,1,0;kq_1)}_{\alpha\gamma} A^{(1,0;jk)}_{\alpha\beta} P^{(1,0,0;j)}_{\beta} \rangle, \\ m^{(1,1)}_{\alpha\beta} &= \langle P^{(1,1,0;jq_1)}_{\alpha\gamma} A^{(1,1;j)}_{\alpha\beta} \rangle, \\ m^{(0,1)}_{\alpha\beta} &= \langle P^{(1,0,0;j)}_{\alpha\delta} A^{(0,0;j)}_{\alpha\beta} + P^{(1,0,0;j)}_{\alpha\delta} A^{(1,1;j)}_{\alpha\beta} + A^{(0,1;jk)}_{\alpha\beta} - P^{(1,0,0;j)}_{\alpha\delta} A^{(1,0;jk)}_{\alpha\beta} P^{(1,0,0;k)}_{\beta\eta} \rangle. \end{aligned} \tag{41}$$

Then, replacing the down-scaling relation (20) truncated at the first order of ϵ into the transformed power-like functional (38), which is expressed in components, results to be

$$\begin{aligned} \hat{\Lambda}_m = s\Big(&\frac{1}{2} m^{(0,2)}_{\alpha\beta} s^2 \int_{\mathcal{C}} \hat{Z}_{\alpha} \hat{Z}_{\beta} d\boldsymbol{x} + \frac{1}{2} m^{(2,0)}_{\alpha\beta} \int_{\mathcal{C}} \frac{\partial \hat{Z}_{\gamma}}{\partial x_{r_1}} \frac{\partial \hat{Z}_{\zeta}}{\partial x_{q_1}} d\boldsymbol{x} + \\ &+ m^{(1,0)}_{\alpha\beta} \int_{\mathcal{C}} \frac{\partial \hat{Z}_{\gamma}}{\partial x_{q_1}} \hat{Z}_{\beta} d\boldsymbol{x} + \frac{1}{2} m^{(0,1)}_{\alpha\beta} \int_{\mathcal{C}} \hat{Z}_{\alpha} \hat{Z}_{\beta} d\boldsymbol{x} - \int_{\mathcal{C}} \hat{Z}_{\alpha} \hat{g}_{\alpha} d\boldsymbol{x}\Big) - s \frac{1}{2} m^{(1,1)}_{\alpha\beta} \int_{\mathcal{C}} \frac{\partial \hat{Z}_{\gamma}}{\partial x_{q_1}} \hat{Z}_{\beta} d\boldsymbol{x} + O(\epsilon). \end{aligned} \tag{42}$$

By applying the stationarity condition to the first variation of the functional (42), $\delta\hat{\Lambda}_m(\hat{\boldsymbol{Z}}, \delta\hat{\boldsymbol{Z}}) = 0$, the deriving Euler–Lagrange equations, which correspond to the field equations of the equivalent first-order medium, can be determined as

$$\boldsymbol{m}^{(2,0)} \frac{\partial^2 \hat{\boldsymbol{Z}}}{\partial x_r^2} - s^2 \boldsymbol{m}^{(0,2)} \hat{\boldsymbol{Z}} - \boldsymbol{m}^{(1,0)} \frac{\partial \hat{\boldsymbol{Z}}}{\partial x_r} - s\boldsymbol{m}^{(1,1)} \frac{\partial \hat{\boldsymbol{Z}}}{\partial x_r} - s\boldsymbol{m}^{(0,1)} \hat{\boldsymbol{Z}} + \hat{\boldsymbol{g}} = \boldsymbol{0}, \tag{43}$$

where It is worth remarking that the variational-asymptotic scheme at the first order provides the governing equation (43) that characterizes a first-order continuum. This approach is able to achieve the same results as those obtained through the procedures exposed in the previous sections.

4 Illustrative applications

In this section, two illustrative examples are presented. In the first one, the asymptotic homogenization approach will be employed to investigate both free and forced wave propagation in a thermo-viscoelastic layered periodic material. In the second example, a periodic microstructured thermo-viscoelastic heterogeneous material representative of a fiber reinforced polymer composite is considered, for which the numerical solution obtained under specific boundary conditions is compared with the analytical one calculated for the corresponding homogeneous material. The first set of examples is aimed at assessing the reliability of the proposed homogenization model. To this end, the parameters have been selected to be consistent from an engineering point of view. On the other hand, in the second example, the numerical values are drawn from specific materials.

4.1 Dispersive properties and transient response of a thermo-viscoelastic laminate

In this section, a comparative study is performed between the analytical results obtained through the Floquet-Bloch theory and those derived from the homogenization model shown in Section 3. The investigation concerns a two-dimensional, infinite, bi-phasic, layered thermo-viscoelastic material. The material exhibits orthotropic phases with the orthotropy axis parallel to the direction $\boldsymbol{e}_1$. The wave propagation takes place along the $\boldsymbol{e}_2$ direction, meaning that $k_1 = 0$. The body is made of two periodically distributed layers with thicknesses $\mathfrak{s}_1$ and $\mathfrak{s}_2$, such that the microstructural length is $\epsilon = d_2 = \mathfrak{s}_1 + \mathfrak{s}_2$, and the thickness ratio is defined as $\eta = \mathfrak{s}_1/\mathfrak{s}_2$. In this mathematical framework, the tensors introduced in (1a)-(1b) are recast in terms of a Prony series as

$$\boldsymbol{h}(\boldsymbol{x},t) = \boldsymbol{h}^{(\infty)}(\boldsymbol{x})\Big(1 + \sum_{n\in\mathbb{N}_{>0}} \chi^n \exp\Big(-\frac{t}{\tau_r^n(\boldsymbol{x})}\Big)\Big), \tag{44}$$

where $\boldsymbol{h}^{(\infty)}$ is the long term material response, χ^n is the $n-$th viscosity ratio of the relaxation functions and $\tau_r^n(\boldsymbol{x})$ is the n-th relaxation time. The bilateral Laplace transform applied to (44) yields

$$\hat{\boldsymbol{h}} = \boldsymbol{h}^{(\infty)}(\boldsymbol{x})\Big(\frac{1}{s} + \sum_{n\in\mathbb{N}_{>0}} \frac{\chi^n \tau_r^n(\boldsymbol{x})}{s\tau_r^n(\boldsymbol{x}) + 1}\Big). \tag{45}$$

Without loss of generality, the relaxation time and the viscosity ratio are assumed to be the same for both phases, and the dimensionless parameters and variables that occur in this example are

$$\begin{array}{llll}
\bar{s} = \frac{s}{s_\zeta}, & \bar{\tau}_r = \tau_r s_\zeta, & \bar{t} = t s_\zeta, & s_\zeta = \frac{1}{\epsilon}\sqrt{\frac{G_{2222}^{(1,\infty)}}{\rho^{(1)}}}, \\
r_K = \frac{K_{22}^{(2,\infty)}}{K_{22}^{(1,\infty)}}, & r_G = \frac{G_{2222}^{(2,\infty)}}{G_{2222}^{(1,\infty)}}, & r_p = \frac{p^{(2,\infty)}}{p^{(1,\infty)}}, & r_\rho = \frac{\rho^{(2)}}{\rho^{(1)}}, \\
\phi^{(1)} = \frac{\alpha_{22}^{(1,\infty)} d_2 \sqrt{G_{2222}^{(1,\infty)}/\rho^1}}{\tilde{K}_{22}^{(1,\infty)}}, & \psi^{(1)} = \frac{p^{(1,\infty)}\theta_0 d_2 \sqrt{G_{2222}^{(1,\infty)}/\rho^1}}{\tilde{K}_{22}^{(1,\infty)}}, & \bar{\hat{U}}_i = \frac{\hat{U}_i}{\epsilon}, & \bar{x}_2 = \frac{x_2}{\epsilon}, \\
\phi^{(2)} = \frac{\alpha_{22}^{(2,\infty)} d_2 \sqrt{G_{2222}^{(1,\infty)}/\rho^1}}{\tilde{K}_{22}^{(2,\infty)}}, & \gamma^{(1)} = \frac{\alpha_{22}^{(1,\infty)}\theta_0}{G_{2222}^{(1,\infty)}}, & \gamma^{(2)} = \frac{\alpha_{22}^{(2,\infty)}\theta_0}{G_{2222}^{(2,\infty)}}, & \bar{\hat{\Theta}} = \frac{\hat{\Theta}}{T_0},
\end{array} \tag{46}$$

with $i = 1, 2$, $\bar{\tau}_r = \frac{1}{2}$, $\chi = \frac{1}{10}$, $\eta = 1$, $r_K = 3$, $r_G = 2$, $r_p = 3$, and $r_\rho = 2$. Then, one has $\gamma^{(1)} = \frac{1}{10}$, $\gamma^{(2)} = \frac{1}{100}$, $\phi^{(1)} = \frac{1}{10}$, $\phi^{(2)} = \frac{1}{100}$, and $\psi^{(1)} = 1$, where the superscripts denote the different phases. The results emphasize the dual behavior of a viscoelastic material, which is expressed through the complex parameter s, where its real component is associated with time attenuation (temporal damping), while its imaginary component governs the propagation characteristics of dispersive Bloch waves. Assuming the source terms as zero and reformulating the dimensionless complex frequency $\bar{s}$ as $\bar{s} = \iota\bar{\omega}$, where $\bar{\omega}$ is the dimensionless real-valued angular frequency, the Floquet-Bloch theory, as presented in [48], can be applied to derive the complex frequency spectrum of the periodic heterogeneous thermo-viscoelastic material.

In Figure 1-(a), the coupled compressional-thermal waves of the heterogeneous material (red) are compared with those obtained by truncating equation (23) at different orders of ϵ: zeroth (yellow), second (green), fourth (blue), and eighth (pink). It is worth noting that, as the truncation order goes up, the approximation shows a significant agreement with the heterogeneous solution. Therefore, the homogenization method

can accurately capture the material response in the low-frequency regime. Figure 1-(b) presents a two-dimensional representation of the dispersion curves in the $(\bar{\omega}, \mathrm{Re}(k_2\epsilon))$ plane. In this context, the lower branches of the spectrum, which govern the propagation of spatially damped dispersive thermoelastic waves within the periodic medium, can be identified. The approximate and analytical frequency spectra are shown in Figures 1-(c) and 1-(d), respectively, using toroidal and cylindrical coordinates. These graphs highlight the excellent agreement between the models within the selected range of the dimensionless angular frequency $\bar{\omega} \in [0, 3]$, with the dimensionless time set to $\bar{t} = 10$. It is important to point out that when the branches lie on the manifolds, the corresponding curves describe the propagation of thermo-elastic waves; when the branches exit from the manifold, they characterize the spatial attenuation of progressive or regressive waves in the material for a fixed propagation direction and under the assumption of homogeneous waves. It should finally be noted that the two representations are equivalent.

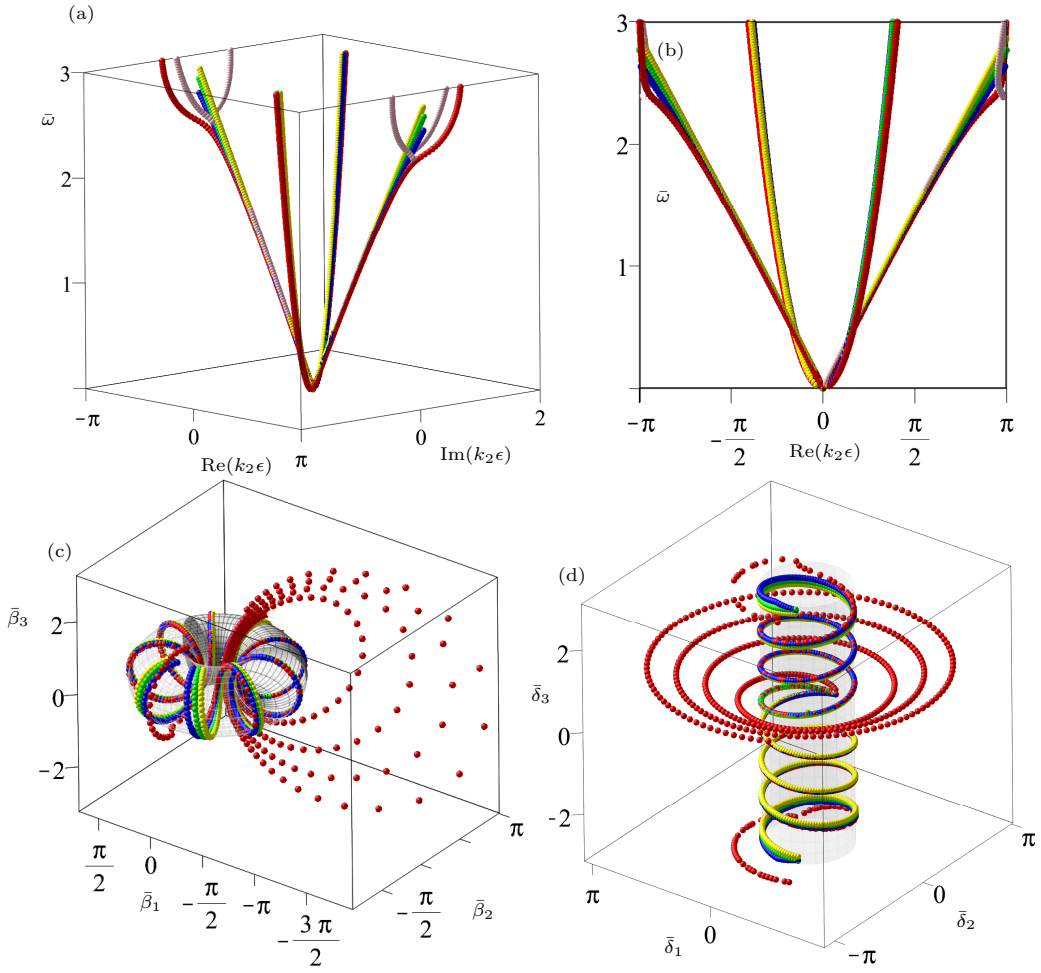

Figure 1: Three-dimensional heterogeneous frequency spectrum (in red) compared with approximate spectra at different orders of the microstructural length ϵ: zeroeth order (yellow), second order (green), fourth order (blue), and eighth order (pink) (a). Two-dimensional projection (b). Comparison between the heterogeneous and approximate complex spectra represented using toroidal coordinates (c) and cylindrical coordinates (d). Branches on the manifolds denote propagating thermo-elastic waves, while those leaving the manifold indicate spatially attenuated homogeneous waves. The parameters used are: $r_K = 3$, $r_p = 5$, $r_G = r_\rho = 2$, $\gamma^{(1)} = \phi^{(1)} = \frac{1}{10}$, $\gamma^{(2)} = \phi^{(2)} = \frac{1}{100}$, $\psi^{(1)} = 1$, $\chi = \frac{1}{10}$, $\bar{\tau}_r = \frac{1}{2}$, and $\eta = 1$.

The relations between the toroidal, cylindrical, and Cartesian coordinates are expressed as

$$\begin{aligned} &\bar{\beta}_1 = \frac{\sinh\left(\left|\bar{\lambda}_j\right|\right)\cos(\arg(\bar{\lambda}_j))}{\cosh\left(\left|\bar{\lambda}_j\right|\right) - \cos(\arg(\bar{\kappa}))}, \quad \bar{\beta}_2 = \frac{\sinh\left(\left|\bar{\lambda}_j\right|\right)\sin(\arg(\bar{\lambda}_j))}{\cosh\left(\left|\bar{\lambda}_j\right|\right) - \cos\left(\arg(\bar{\kappa})\right)}, \quad \bar{\beta}_3 = \frac{\sin(\arg(\bar{\kappa}))}{\cosh\left(\left|\bar{\lambda}_j\right|\right) - \cos\left(\arg(\bar{\kappa})\right)}, \\ &\bar{\delta}_1 = \left|\bar{\lambda}_j\right| \cos\left(\arg(\bar{\kappa})\right)), \qquad \bar{\delta}_2 = \left|\bar{\lambda}_j\right| \sin\left(\arg(\exp(\bar{\kappa}))\right), \quad \bar{\delta}_3 = \mathrm{Re}(\bar{k}_j), \end{aligned} \tag{47}$$

with $\bar{\lambda}_j = \exp(\iota \bar{k}_j)$, $\bar{\kappa} = \exp(\iota \bar{\omega} \bar{t})$ and $j = 1, 2$. Figure 4 presents the compressional wave dispersion curves for the heterogeneous material, obtained via Floquet-Bloch theory, along with those derived from the homogenization model by truncating the governing average field equation at various orders of the microstructural length ϵ, in the limiting case of vanishing phase relaxation times. The spectra corresponding to the heterogeneous material are shown in red. Panel 4-(a) displays the results using a second order approximation (in green); panels 4-(b) and 4-(c) show the fourth order (in blue) and the sixth order (in red) approximations, respectively, within the frequency range $\bar{\omega} \in [0, 25]$. Finally, a zoomed view of the panel 4-(c) is visible in figure 4-(d). Figure 4-(e) illustrates the propagation of the thermal wave for either the material (yellow) derived with the homogenization method at the second order (29) or the heterogeneous material (red) obtained by means of the Floquet-Bloch theory. The dark red and dark yellow curves recognize the translations of the respective dispersion curves due to the periodicity of the material along $\boldsymbol{e}_2$ around $\mathrm{Re}(k_2\epsilon)$. A two-dimensional view in the $(\mathrm{Im}(k_2\epsilon), \bar{\omega})$-plane can be seen in figure 4-(f). In the Panel, the comparison emphasizes the excellent agreement between the two methods. Therefore, through an asymptotic homogenization technique, and by controlling the truncation order, it is possible to capture not only the acoustic branches but also the optical branches of the dispersion spectrum of the material. In [49], it was shown that the continualization scheme applied to the layered material led to a convergent approximation of the entire spectrum, and that the intercepts of the branches at the wavenumbers about which the expansion of the integral operators is performed coincide with those of the heterogeneous material. The asymptotic homogenization approach enable to tend it as the truncation order increases. Indeed, higher-order expansions lead to gradient-type field equations exhibiting the same mathematical structure with nonlocal inertial terms, which play a fundamental role in the consistent characterization of the dispersive behavior of heterogeneous materials. To face the forced wave propagation problem, the material is supposed to be subjected to $\mathcal{C}$-periodic harmonic source terms with period $\mathcal{C} = [0, L] \times [0, \delta L]$ in the physical space and complex frequency domain, applied in the direction of the axis x_q, as $\hat{\boldsymbol{g}}(x_q) = \boldsymbol{g} \exp\left(\iota 2\pi n \frac{x_q}{L}\right) = (\hat{b}_1\ \hat{b}_2\ \hat{r})^{\mathrm{T}} \exp\left(\iota 2\pi n \frac{x_q}{L}\right)$, with $q = 1, 2$, $n \in \mathbb{Z}$ and $\boldsymbol{g} \in \mathbb{C}^3$. Since L is a large multiple of ϵ, it can be considered a representative portion of the overall body. This fact implies that the source terms are characterized by a period much larger than the microstructural size ϵ. It must be observed that applying the inverse Laplace transform to the source terms that are collected in the vector $\hat{\boldsymbol{g}}(x_q)$ provides a spatially harmonic and temporally impulsive structure in $\bar{t} = 0$. Replacing the expression of the source terms into the average field equation of infinite order (22) enables us to derive the solution at the macroscale in the physical space and in the complex domain as

$$\hat{\boldsymbol{Z}}(x_q, s) = \Big(\sum_{j \in \mathbb{N}} \epsilon^{(2j)} \boldsymbol{C}^{(2j)}(x_q, s) \Big)^{-1} \hat{\boldsymbol{g}}(x_q). \tag{48}$$

In figures 2-(a) and (b), the real and imaginary parts of the dimensionless macro displacement component $\bar{\hat{U}}_2$ are shown with respect to the real and imaginary parts of the dimensionless complex frequency $\bar{s}$.

The macro displacement component $\bar{\hat{U}}_2$ can be derived by solving the equation (48), truncating it at the second order of ϵ with $j = 1$, and considering the non-null component $\hat{b}_2$. In figures 2-(c) and (d), the magnitude of the dimensionless macro displacement component $\bar{\hat{U}}_2$ is represented with respect to dimensionless frequency $\bar{\omega}$ by increasing the dimensionless relaxation time $\bar{\tau}_r$ as $\frac{1}{5}$ (blue) and $\frac{1}{2}$ (green) and the dimensionless amplitude of source term $\hat{\bar{b}} = \frac{\hat{b}}{G_{2222}^{(1,\infty)}}$ as 10 (green) and 50 (blue), respectively. Moreover, in figures 2-(e) and (f), the magnitude of the dimensionless macro displacement component $\bar{U}_2$ that is recast in the physical space and in the time domain is represented with respect to dimensionless time by changing the dimensionless relaxation time $\bar{\tau}_r$, the viscosity χ and the parameter $\bar{b}$. It can be observed that, as the relaxation time arises, there is a remarkable decrease in the trend of the resulting curves.
In figures 3-(a) and (b), the real and imaginary components of the dimensionless macro temperature $\bar{\hat{\Theta}}$ are shown in terms of the real and imaginary parts of the dimensionless complex frequency $\bar{s}$. The macro temperature $\bar{\hat{\Theta}}$ can be obtained by truncating the equation (48) at the zeroth order of ϵ with $j = 0$, and taking into account the non-null source term $\hat{r}$. Considering the dimensionless amplitude of source term $\hat{r}$ as $\bar{\hat{r}} = \frac{\hat{r} T_0}{G_{2222}^{(1,\infty)} s_\zeta}$, figures 3-(c) and (d) display the real and imaginary parts of macro temperature $\bar{\Theta}$ converted in the physical space and in the time domain, respectively.

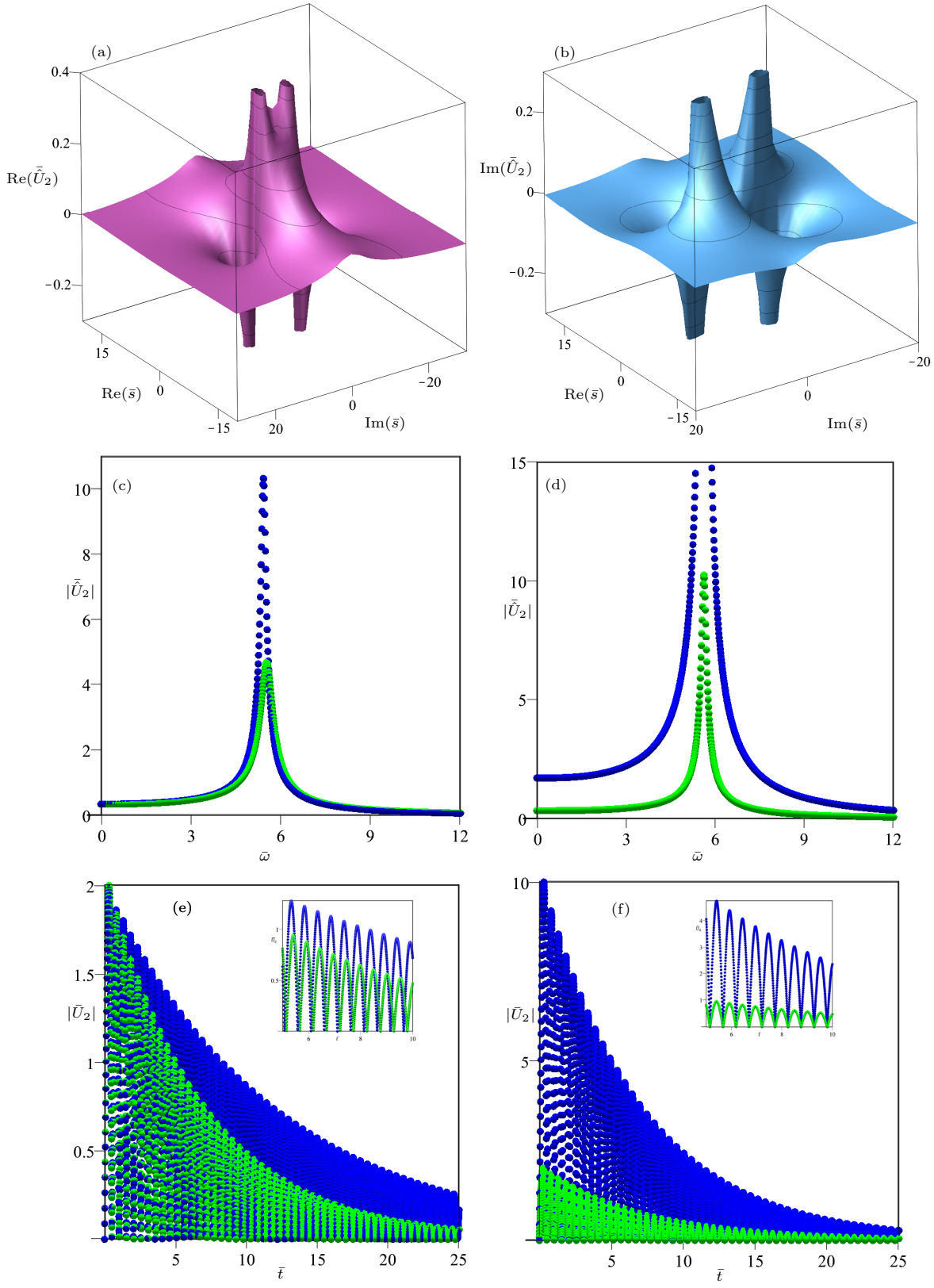

Figure 2: Real (a) and imaginary (b) parts of the dimensionless macro–displacement component $\bar{\hat{U}}_2$ as functions of the real and imaginary parts of the dimensionless complex frequency $\bar{s}$. Magnitude of $\bar{\hat{U}}_2$ versus the dimensionless angular frequency $\bar{\omega}$ for $\bar{\tau}_r = \frac{1}{5}$ (blue) and $\frac{1}{2}$ (green) (c), and for $\bar{b} = 50$ (blue) and 10 (green) (d). Magnitude of $\bar{U}_2$ versus the dimensionless time $\bar{t}$ for varying $\bar{\tau}_r$ (e) and $\bar{b}$ (f).

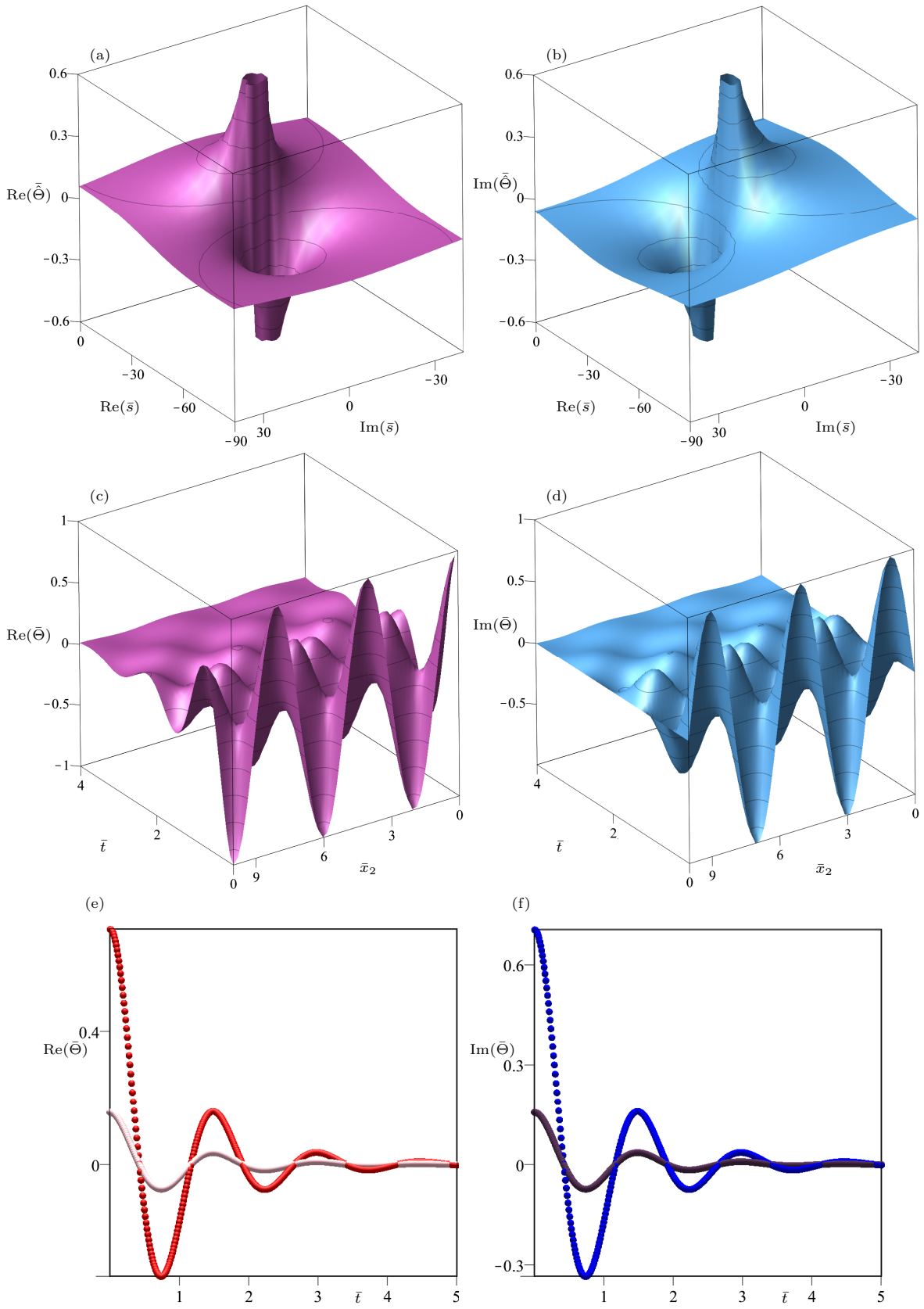

Figure 3: Real (a) and imaginary (b) parts of the dimensionless macro temperature $\bar{\bar{\Theta}}$ as functions of the real and imaginary parts of the dimensionless complex frequency $\bar{s}$. Real (c) and imaginary (d) parts of $\bar{\Theta}$ versus the dimensionless time $\bar{t}$ and $\bar{x}_2$. Real part of $\bar{\Theta}$ and imaginary part of $\bar{\Theta}$ versus the dimensionless time for $\bar{x}_2 = \frac{1}{2}$ (red) and $\frac{1}{10}$ (pink) (e), and for $\bar{x}_2 = \frac{1}{2}$ (blue) and $\frac{1}{10}$ (violet) (f).

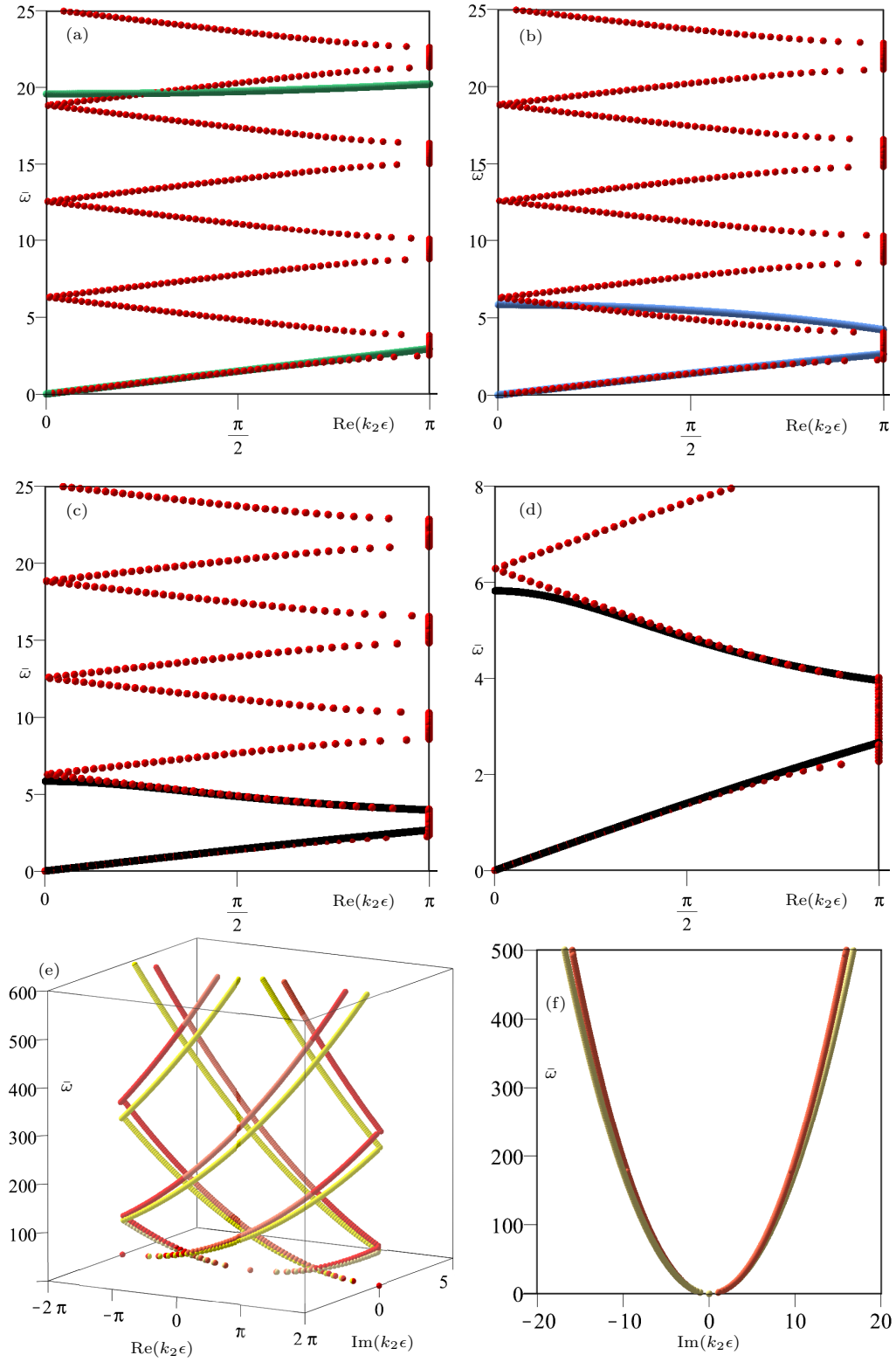

Figure 4: Two-dimensional heterogeneous frequency complex spectra (in red) compared with those obtained using the homogenization method at different orders of the microstructural length ϵ associated with elastic wave propagation: (a) second order approximation (green); (b) fourth order (blue); (c) sixth order (black); (d) zoomed-in view of subfigure (c). The used parameters are $r_G = r_\rho = 2$ and $\eta = 1$. Three dimensional heterogeneous translated frequency spectra (red) vs. those related to the homogenization method (yellow) associated to thermal waves (e), view in the $(\mathrm{Im}(k_2\epsilon), \bar{\omega})$-plane (f).The parameters used are: $r_K = 3$, $\chi = \frac{1}{10}$, $\bar{\tau}_r = \frac{1}{2}$, and $\eta = 1$.

Finally, a two-dimensional view of the real and imaginary parts of $\bar{\Theta}$ is shown in figures 3-(e) and (f), respectively, by varying the dimensionless time $\bar{t}$ and setting the dimensionless coordinate $\bar{x}_2$ as $\frac{1}{2}$ (red) and $\frac{1}{10}$ (pink) (e) and $\frac{1}{2}$ (blue) and $\frac{1}{10}$ (violet) (f).

4.2 Frequency-dependent response of a thermo-viscoelastic periodic material with a complex microstructure

A bi-phase, two-dimensional, infinite periodic medium is considered, obtained through the spatial repetition of a representative periodic cell along the two periodicity vectors $\mathbf{e}_1$ and $\mathbf{e}_2$. The periodic cell consists of a central square-shaped inclusion with side length $\epsilon/2$ embedded in a matrix. The square inclusion is assumed to consist of carbon fiber, characterized by a Young's modulus of $E^{(i)} = 240$ GPa, Poisson's coefficient $\nu^{(i)} = 0.28$, mass density $\rho^{(i)} = 1950\,\mathrm{kg/m^3}$, coefficient of thermal expansion $\varphi^{(i)} = 6.7 \cdot 10^6 \mathrm{N/(m^2K)}$, thermal conductivity $\tilde{V}^{(i)} = 50\,\mathrm{W/(m\,K)}$, and a specific heat at constant strain $\tilde{m}^{(i)} = 900\,\mathrm{N/(m^2K)}$. The matrix, instead, is made of epoxy resin characterized by a Young modulus $E^{(m)} = 3.5$ GPa, Poisson's coefficient $\nu^{(m)} = 0.35$, mass density $\rho^{(m)} = 1300\,\mathrm{kg/m^3}$, thermal expansion coefficient $\varphi^{(m)} = 2.7 \cdot 10^5$ N/(m^{2}K), thermal conductivity $\tilde{V}^{(m)} = 5\,\mathrm{W/(m\,K)}$, and constant $\tilde{m}^{(m)} = 900\,\mathrm{N/(m^2K)}$. Relaxation function form of time-dependent micro constitutive properties is again expressed according to eq. (44) with $n = 1$, $\chi = 1$ for both phases, $\tau_r^{(m)} = 0.1$ s for the matrix and $\tau_r^{(i)} = 0.01$ s for the inclusion. Both phases are assumed to exhibit an isotropic behavior, and a plane stress state is considered for which $\boldsymbol{\sigma}\mathbf{e}_3 = \mathbf{0}$ and $\mathbf{q}\mathbf{e}_3 = 0$, being $\mathbf{e}_3$ the unit vector perpendicular to $\mathbf{e}_1$ and $\mathbf{e}_2$ in a right-handed reference system. Therefore, the long-term, non-vanishing components of microscopic tensors can be expressed, for both phases, as

$$G_{1111}^{(\infty)} = G_{2222}^{(\infty)} = \frac{E}{1-\nu^2},\ G_{1122}^{(\infty)} = \frac{\nu E}{1-\nu^2},\ G_{1212}^{(\infty)} = \frac{E}{2(1+\nu)},\ V_{11}^{(\infty)} = V_{22}^{(\infty)} = V,\ \varphi_{11}^{(\infty)} = \varphi_{22}^{(\infty)} = \varphi\frac{1-2\nu}{1-\nu}. \tag{49}$$

Considering $s = i\omega$, the frequency $\omega \in \mathbb{R}$ has been discretized into a finite number of points, and consequently, the frequency-dependent perturbation functions have been numerically computed as finite elements solutions of the cell problems at the order ϵ^{-1}, as described in Section 3.1. Once the perturbation functions are obtained, it is possible to determine, for each value of ω, the components of the overall constitutive tensors in the transformed space using eq.s (41). Fig.s 5-(a) and (b) show the real and imaginary parts, respectively, of the dimensionless component $\bar{\hat{C}}_{1111} = \frac{\hat{C}_{1111}}{E^{(i)}}$ of the overall elastic tensor. They are plotted as functions of dimensionless frequency $\bar{\omega} = \omega/\omega_\zeta$ with $\omega_\zeta = \frac{1}{\epsilon}\sqrt{\frac{G_{1111}^{(i,\infty)}}{\rho^{(i)}}}$. All the global constitutive constants exhibit the same qualitative behavior as the frequency varies. Therefore, only one of them has been represented. Assuming an unbounded two-dimensional thermo-viscoelastic domain, neglecting the inertial contributions, and considering the pseudo-static homogeneous equations at the macroscale of a first-order homogenized continuum

$$\hat{C}_{lr_1pq_1}^m(\omega)\frac{\partial^2 \hat{U}_p(\omega)}{\partial x_{q_1}\partial x_{r_1}} - \hat{\alpha}_{lq_1}^m(\omega)\frac{\partial \hat{\Theta}(\omega)}{\partial x_{q_1}} = 0, \tag{50a}$$

$$\hat{K}_{r_1q_1}^m(\omega)\frac{\partial^2 \hat{\Theta}(\omega)}{\partial x_{r_1}\partial x_{q_1}} = 0, \tag{50b}$$

where the transformed tensor components are ω-dependent and defined as $\hat{C}_{ijhk}^m(\omega) = i\omega\hat{G}_{ijhk}^m(\omega)$, $\hat{\alpha}_{ij}^m(\omega) = i\omega\hat{\psi}_{ij}^m(\omega)$, and $\hat{K}_{ij}^m(\omega) = i\omega\hat{V}_{ij}^m(\omega)$, one possible solution of system (50) reads

$$\hat{U}_1(\omega) = \tilde{\eta}_{111}(\omega)x_1^2 + 2\,\eta_{112}x_1x_2 + \eta_{122}x_2^2 + \beta_{11}x_1 + \beta_{12}x_2, \tag{51a}$$

$$\hat{U}_2(\omega) = \tilde{\eta}_{222}(\omega)x_2^2 + 2\,\eta_{221}x_1x_2 + \eta_{211}x_1^2 + \beta_{12}x_1 + \beta_{22}x_2, \tag{51b}$$

$$\hat{\Theta} = x_1\xi_1 + x_2\xi_2, \tag{51c}$$

where η_{iij}, η_{jii}, ξ_j, β_{jj}, with $i, j = 1, 2$ are problem parameters and the auxiliary quantities $\tilde{\eta}_{111}$ and $\tilde{\eta}_{222}$ are expressed in terms of them and of the transformed tensor components as

$$\tilde{\eta}_{111}(\omega) = -\frac{1}{2}\,\frac{2\,\hat{C}_{1122}(\omega)\eta_{221} + 2\,\hat{C}_{1212}(\omega)\eta_{122} + 2\,\hat{C}_{1212}(\omega)\eta_{221} - \hat{\alpha}_{11}(\omega)\xi_1}{\hat{C}_{1111}(\omega)}, \tag{52a}$$

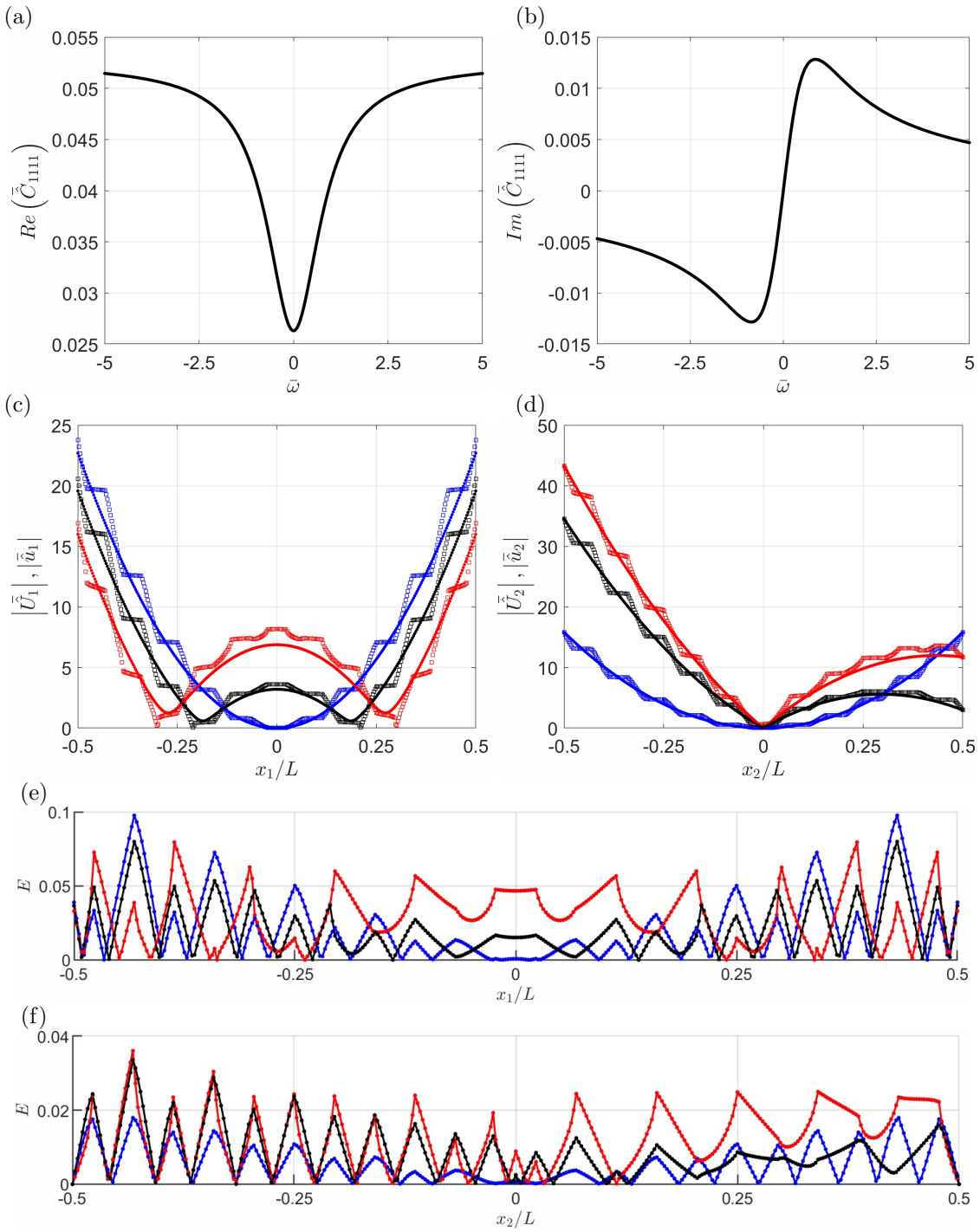

Figure 5: Real (a) and imaginary (b) parts of the dimensionless component $\bar{\hat{C}}_{1111}$ vs the dimensionless frequency $\bar{\omega} = \omega/\omega_\zeta$. (c) Magnitude of $\bar{\hat{U}}_1$ (solid) and $\bar{\tilde{u}}_1$ (squares) for $\eta_{122} = \eta_{221} = 10^3$/m, $\xi_1 = \xi_2 = 10^3$ K/m and $\bar{\omega} = 8.3/\omega_\zeta$ as a function of x_1/L at $x_2/L = 0$ (blue), $x_2/L = 1/4$ (red), and $x_2/L = 1/3$ (black). (e) Error $E(\mathbf{x}) = (\bar{\tilde{u}}_1 - \bar{\hat{U}}_1)/\max_{\mathbf{x}} \bar{\tilde{u}}_1$ for the same three sections. (d) Magnitude of $\bar{\hat{U}}_2$ (solid) and $\bar{\tilde{u}}_2$ (squares) for $\eta_{112} = \eta_{221} = 10^3$/m, $\xi_1 = \xi_2 = 10^3$ K/m and $\bar{\omega} = 50/\omega_\zeta$ as a function of x_2/L at $x_1/L = 0$ (blue), $x_2/L = 1/4$ (red), and $x_2/L = 1/3$ (black). (f) Error $E(\mathbf{x}) = (\bar{\tilde{u}}_2 - \bar{\hat{U}}_2)/\max_{\mathbf{x}} \bar{\tilde{u}}_2$ for the same three sections.

$$\tilde{\eta}_{222}(\omega) = -\frac{1}{2} \frac{2\,\hat{C}_{1122}(\omega)\eta_{112} + 2\,\hat{C}_{1212}(\omega)\eta_{211} + 2\,\hat{C}_{2112}(\omega)\eta_{112} - \hat{\alpha}_{22}(\omega)\xi_2}{\hat{C}_{2222}(\omega)}. \tag{52b}$$

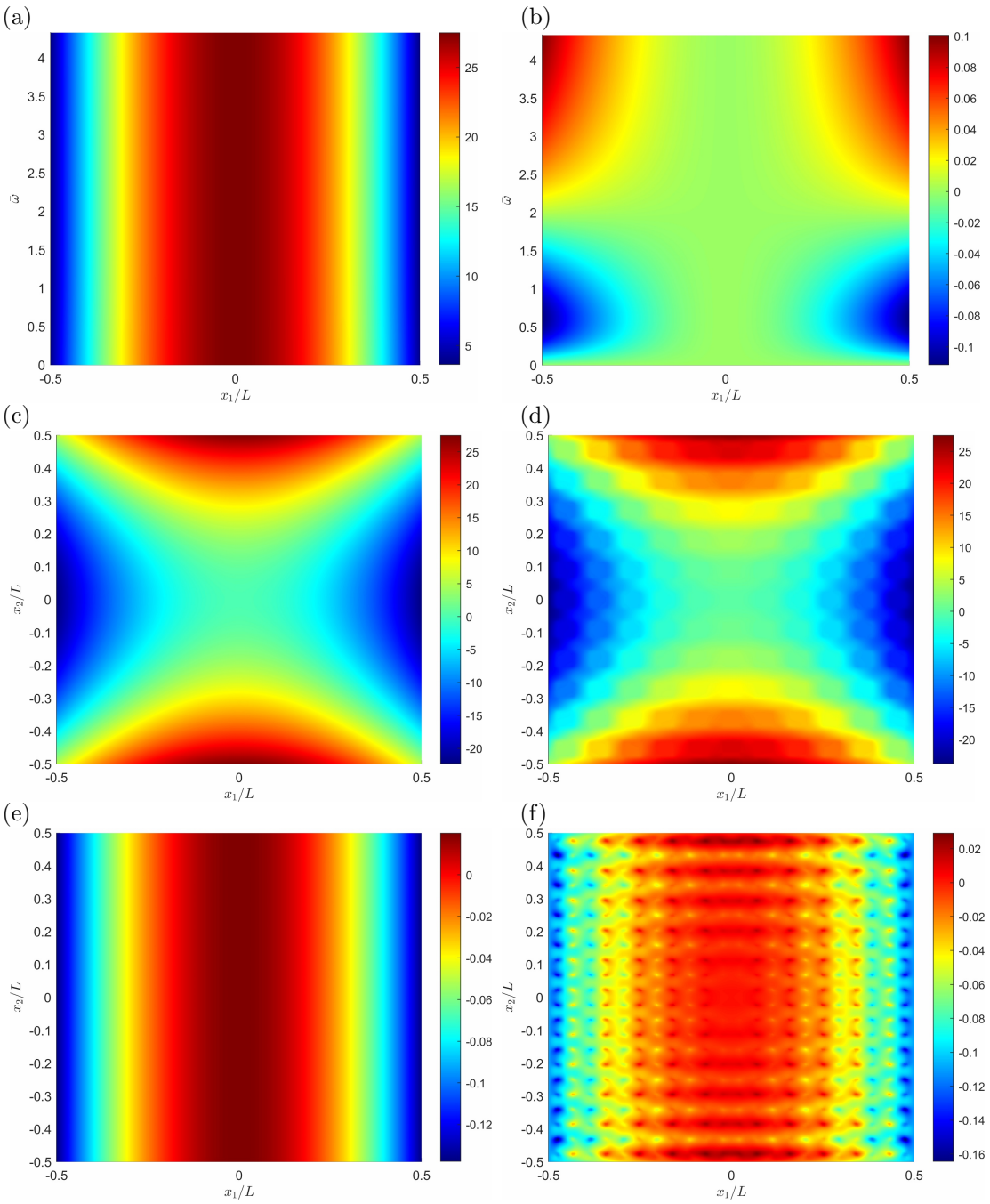

Figure 6: Non vanishing parameters: $\eta_{122}=\eta_{221}=10^3$/m and $\xi_1=\xi_2=10^3$ K/m: (a)Re $\left(\bar{\hat{U}}_1\right)$ vs x_1/L and $\bar{\omega}=\omega/\omega_\zeta$ at $x_2=L/2$; (b) Im $\left(\bar{\hat{U}}_1\right)$ vs x_1/L and $\bar{\omega}$ at $x_2=L/2$; (c) Re $\left(\bar{\hat{U}}_1\right)$ vs x_1/L and x_2/L at $\bar{\omega}=8.3/\omega_\zeta$; (d) Re $\left(\bar{\hat{u}}_1\right)$ vs x_1/L and x_2/L at $\bar{\omega}=8.3/\omega_\zeta$; (e) Im $\left(\bar{\hat{U}}_1\right)$ vs x_1/L and x_2/L at $\bar{\omega}=8.3/\omega_\zeta$; (f) Im $\left(\bar{\hat{u}}_1\right)$ vs x_1/L and x_2/L at $\bar{\omega}=8.3/\omega_\zeta$.

The polynomial solution (51a)-(51c) is proved to be valid at the macroscale for an infinite domain and for a finite square subdomain of length L, once the appropriate Dirichlet boundary conditions are provided. These last are the eq.s (51a)-(51c) evaluated along the boundary of the finite cluster domain $\mathcal{C}$. Figure 6 shows a comparison between the solution (51a)-(51c) of the homogenized medium and the one numerically obtained by considering a heterogeneous system made by a cluster of 11×11 cells. In particular, the

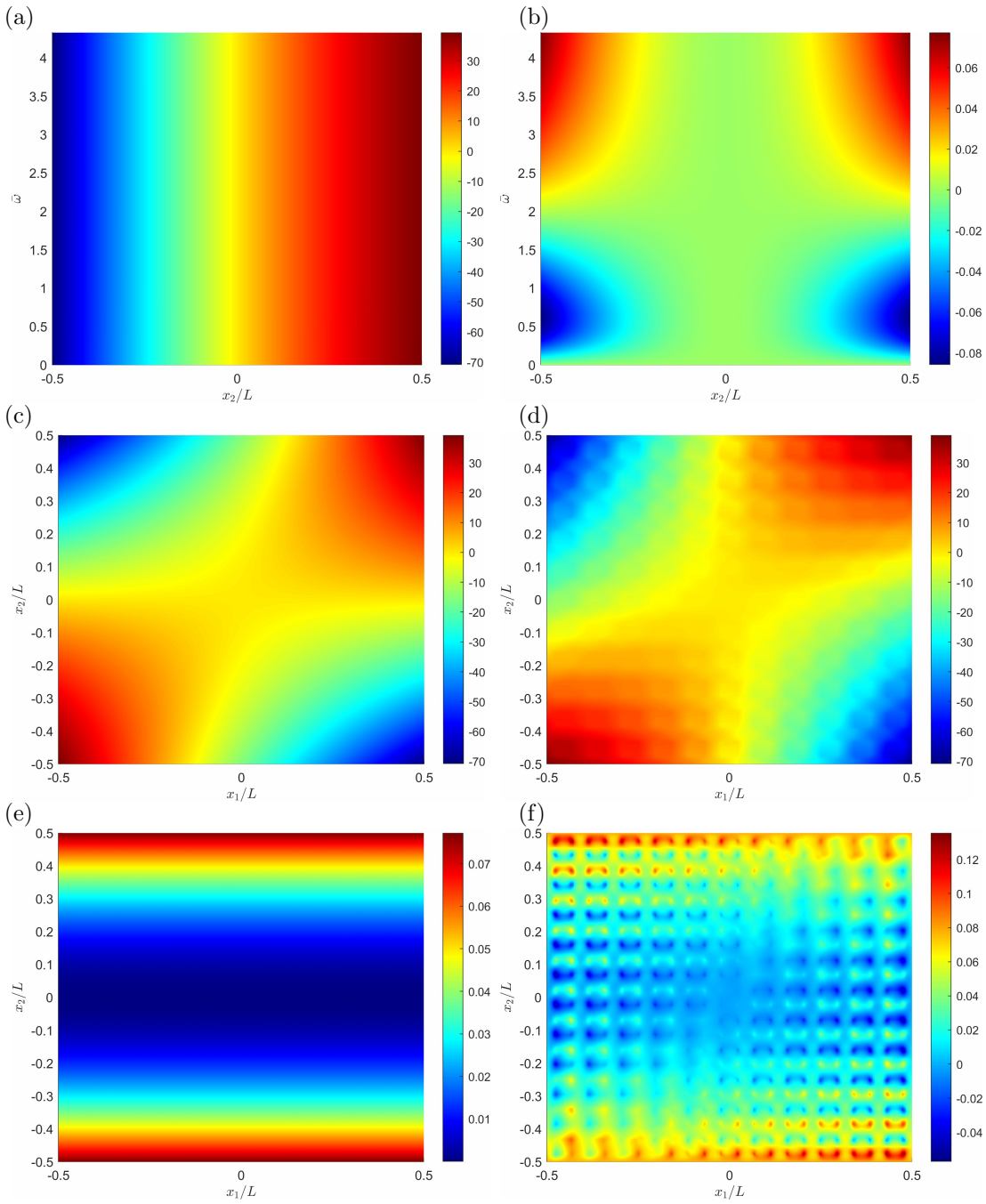

Figure 7: Non-vanishing parameters: $\eta_{112}=\eta_{221}=10^3$/m and $\xi_1=\xi_2=10^3$ K/m: (a)Re $\left(\bar{\hat{U}}_2\right)$ vs x_2/L and $\bar{\omega}=\omega/\omega_\zeta$ at $x_1=L/2$; (b) Im $\left(\bar{\hat{U}}_2\right)$ vs x_2/L and $\bar{\omega}$ at $x_1=L/2$; (c) Re $\left(\bar{\hat{U}}_2\right)$ vs x_1/L and x_2/L at $\bar{\omega}=50/\omega_\zeta$; (d) Re $\left(\bar{\hat{u}}_2\right)$ vs x_1/L and x_2/L at $\bar{\omega}=50/\omega_\zeta$; (e) Im $\left(\bar{\hat{U}}_2\right)$ vs x_1/L and x_2/L at $\bar{\omega}=50/\omega_\zeta$; (f) Im $\left(\bar{\hat{u}}_2\right)$ vs x_1/L and x_2/L at $\bar{\omega}=50/\omega_\zeta$.

following non-vanishing set of parameters is taken into account: $\eta_{122}=\eta_{221}=10^3$/m, $\xi_1=\xi_2=10^3$K/m. Subfigures 6-(a) and 6-(b) plot the real and imaginary components of dimensionless horizontal displacement $\bar{\hat{U}}_1=\hat{U}_1/L$, chosen as the representative quantity to plot for this set of parameters, for a fixed $x_2=L/2$ as functions of x_1/L and $\bar{\omega}$. If one chooses, without losing generality, the frequency $\bar{\omega}=8.3/\omega_\zeta$, subfigure 6-(c)

represents the real component of $\bar{\hat{U}}_1$ over the entire cluster, and the subfigure 6-(d) is the heterogeneous counterpart. Analogously, subfigure 6-(e) plots the imaginary component of the homogenized solution $\bar{\hat{U}}_1$ and the subfigure 6-(f) plots the heterogeneous one. In addition, figure 5-(c) shows the magnitude of the transformed dimensionless horizontal displacement at the frequency $\bar{\omega} = 8.3/\omega_\zeta$, for three different values of x_2/L, namely $x_2/L = 0$ (blue curve), $x_2/L = 1/4$ (red curve), and $x_2/L = 1/3$ (black curve), both for the analytical solution (51a), plotted with a solid line and for the solution obtained numerically over the heterogeneous domain (squared markers). After defining the error $E(\mathbf{x}) = (\bar{\hat{u}}_1 - \bar{\hat{U}}_1)/\max_{\mathbf{x}}\bar{\hat{u}}_1$, fig. 5-(e) shows such a quantity for the same three section. It remains under 10% at all the points examined. A mean error defined as $||\bar{\hat{u}}_1 - \bar{\hat{U}}_1||_{L_2}/\max_{\mathbf{x}}\bar{\hat{u}}_1$ gives 3.1% for $x_2/L = 0$, 3.4% for $x_2/L = 1/4$ and 2.6% for $x_2/L = 1/3$. It is worth noting that the error has been computed considering the macroscopic and microscopic fields, and that significantly higher accuracy can be achieved by performing the down-scaling procedure starting from the macroscopic solution. Figure 7 refers to a different set of non-vanishing parameters, namely $\eta_{112} = \eta_{221} = 10^3$/m and $\xi_1 = \xi_2 = 10^3$K/m, for which the dimensionless vertical displacement $\bar{\hat{U}}_2 = \hat{U}_2/L$ is chosen as the representative quantity to plot in order to assess the validity of the first-order homogenization procedure. Fixing $x_1 = L/2$, subfigures 7-(a) and (b) show the real and imaginary components of $\bar{\hat{U}}_2$ as functions of x_2/L and $\bar{\omega}$. Subfigure 7-(c) is the representation of $\mathrm{Re}\left(\bar{\hat{U}}_2\right)$ at $\bar{\omega} = 50/\omega_\zeta$ over the whole cluster and subfigure 7-(d) plots the real component of the solution numerically obtained over the heterogeneous cluster at the same fixed frequency. Finally, subfigures 7-(e) and (f) plot the imaginary component of the transformed vertical displacement for the homogeneous and heterogeneous domains, respectively, again at the same fixed frequency $\bar{\omega} = 50/\omega_\zeta$. Similarly to what was done for the previous set of parameters, the magnitude of the dimensionless transformed vertical displacement $\bar{\hat{U}}_2$ (solid line) and $\bar{\hat{u}}_2$ (squared markers), is plotted for this second set of parameters in figure 5-(d) at the fixed frequency $\bar{\omega} = 50/\omega_\zeta$, for three different values of x_1/L, namely $x_1/L = 0$ (blue curve), $x_1/L = 1/4$ (red curve), and $x_1/L = 1/3$ (black curve).The error $E(\mathbf{x}) = (\bar{\hat{u}}_2 - \bar{\hat{U}}_2)/\max_{\mathbf{x}}\bar{\hat{u}}_2$ is plotted in figure 5-(f) at the same frequency and for the same three section. It remains below 4% at all the points considered, confirming the effectiveness of the proposed homogenization technique. The mean error $||\bar{\hat{u}}_2 - \bar{\hat{U}}_2||_{L_2}/\max_{\mathbf{x}}\bar{\hat{u}}_2$ gives 0.7% for $x_1/L = 0$, 1.4% for $x_1/L = 1/4$ and 1.1% for $x_1/L = 1/3$. As evident from all the reported cases, an excellent agreement can be achieved between homogeneous and heterogeneous solutions, regardless of the frequency and parameters considered, underscoring the prediction accuracy of the homogenization model.

5 Conclusion and future studies

In the present paper, a novel formulation has been proposed for the analysis of thermo-viscoelastic heterogeneous materials with periodic microstructures using a non-local asymptotic homogenization approach. The theoretical framework relies on a compact matrix operator formulation, which enables to synthetically represent the governing field equations in both the physical space and the complex frequency domain. This structure is clarified through matrix operators that are indexed to indicate the order of the differential operator with respect to the spatial variable, while the second index denotes the corresponding power of the complex frequency. The periodicity of the microstructure and the multidimensional Floquet-Bloch transform have permitted to recast the matrix formulation in the wavevector domain to analyze both the free and the forced wave propagation.

The asymptotic expansion at the microscale of the vector collecting the transformed displacement and temperature fields, with respect to the characteristic size of the microstructure has enabled the perturbative development of the field equations in matrix operator form. This has led to the derivation of recursive differential problem, whose solutions depend on squared algebraic operators involving the perturbation functions, the transformed vector at the macroscale and its gradients. The corresponding cell problems have been solved to determine the perturbation functions. After deriving the average field equations of infinite order, the free wave propagation inside the periodic material has been studied by carrying out truncations at even orders with respect to the characteristic size and leading to several dispersion spectra obtained from the resolution of algebraic problems in the wavevector and frequency complex domain. It has also been shown for a periodic laminated material in the limiting case of vanishing relaxation times that, as the order in the asymptotic homogenization method increases, it is possible to accurately approximate the first optical branch of the spectrum of the corresponding heterogeneous material, in addition to the low-frequency acoustic branches.

For the forced dynamic case, a perturbative technique has been performed by expanding the transformed macroscopic vector with respect to the characteristic size parameter. The accuracy of the proposed model has been assessed through a comparison with the Floquet-Bloch spectrum related to a heterogeneous material. The dispersion curves derived from the homogenized model exhibit excellent agreement with the exact solutions obtained via the Floquet-Bloch theory. The proposed model is a robust tool to investigate the behavior of complex periodic materials, which accurately recovers their coupled viscoelastic and thermal responses. Unlike the high-frequency continualization technique for layered materials previously proposed by the authors, the approximations obtained with the present asymptotic homogenization approach are able to capture the optical branches as the truncation order grows, which improve with higher-order approximations. It is worth emphasizing that, while a very good approximation of the acoustic branches is a well-established result when using such techniques, the ability to approximate the optical branches is a valuable and novel contribution to the current state of the art. These insights pave the way for new perspectives for the modeling of wave propagation in periodic materials and they have the potential to resolve the full dispersion spectrum with the optical branches. Beyond the wave propagation problem, the proposed method is suitable for a wide range of engineering applications such us the identification of frequency band gaps, vibration analysis, and advanced material design. Future developments could extend the present theory to quasi-periodic microstructures and more complex multi-field materials.

Acknowledgments

F. Fantoni and A. Bacigalupo are members of INdAM-GNFM. The authors gratefully acknowledge the National Group of Mathematical Physics (GNFM-INdAM, Italy), the financial support of the European Union – Next Generation EU, under the call PRIN 2022 PNRR of the Italian Minister of University and Research (MUR) - Project P2022HLHHB (PE: Physical Sciences and Engineering): "A digital framework for the cutting of soft tissues: A first step towards virtual surgery" and the financial support of the European Union – Next Generation EU, under the call PRIN 2022 of the Italian Minister of University and Research (MUR) - Project 202222LB37 (PE: Physical Sciences and Engineering): "Advanced Design of avant-garde ACTIVE microstructured materials via additive manufacturing (ADACTIVE)".

References

[1] Ignaczak, J., Ostoja-Starzewski, M. *Thermoelasticity with finite wave speeds*. OUP Oxford, (2009).

[2] Abouelregal, A. E., Marin, M., Foul, A., et al. Coupled responses of thermomechanical waves in functionally graded viscoelastic nanobeams via thermoelastic heat conduction model including atangana–baleanu fractional derivative. Scientific Reports, 14(1), pp. 9122, (2024).

[3] Kovács, R. Heat equations beyond fourier: From heat waves to thermal metamaterials. Physics Reports, 1048, pp. 1–75, (2024).

[4] Ward, I. M., Sweeney, J. *Mechanical properties of solid polymers*. John Wiley & Sons, (2012).

[5] Pettermann, H. E., DeSimone, A. An anisotropic linear thermo-viscoelastic constitutive law: Elastic relaxation and thermal expansion creep in the time domain. Mechanics of Time-Dependent Materials, 22(4), pp. 421–433, (2018).

[6] Tarantino, M., Zerhouni, O., Danas, K. Random 3d-printed isotropic composites with high volume fraction of pore-like polydisperse inclusions and near-optimal elastic stiffness. Acta Materialia, 175, pp. 331–340, (2019).

[7] Xi, M., Yun, G., Narsu, B. A mathematical model for viscoelastic properties of biological soft tissue. Theory in Biosciences, 141(1), pp. 13–25, (2022).

[8] Estermann, S.-J., Pahr, D. H., Reisinger, A. Material design of soft biological tissue replicas using viscoelastic micromechanical modelling. Journal of the Mechanical Behavior of Biomedical Materials, 125, pp. 104875, (2022).

[9] Ahmed, H. M., Salem, N. M., Al-Atabany, W. Human cornea thermo-viscoelastic behavior modelling using standard linear solid model. BMC Ophthalmology, 23(1), pp. 250, (2023).

[10] Ezzat, M. A., Alabdulhadi, M. H. Thermomechanical interactions in viscoelastic skin tissue under different theories. Indian Journal of Physics, 97(1), pp. 47–60, (2023).

[11] Peng, X., Yin, H., Chen, J., et al. A phenomenological thermal-mechanical viscoelastic constitutive modeling for polypropylene wood composites. Advances in Materials Science and Engineering, 2012(1), pp. 793617, (2012).

[12] Song, R., Morak, M., Muliana, A. A thermo-viscoelastic model of anisotropic polyamide short glass fiber composites. Composite Structures, 296, pp. 115850, (2022).

[13] Zhang, J., Lay, R. J., Roberts, S. K., et al. Towards real-time finite-strain anisotropic thermo-visco-elastodynamic analysis of soft tissues for thermal ablative therapy. Computer Methods and Programs in Biomedicine, 198, pp. 105789, (2021).

[14] Muliana, A. H., Sawant, S. Responses of viscoelastic polymer composites with temperature and time dependent constituents. Acta Mechanica, 204(3), pp. 155–173, (2009).

[15] Arash, B., Exner, W., Rolfes, R. A finite deformation phase-field fracture model for the thermo-viscoelastic analysis of polymer nanocomposites. Computer Methods in Applied Mechanics and Engineering, 381, pp. 113821, (2021).

[16] Cheng, H., Wang, J., Huang, Z. A thermo-viscoelastic constitutive model for compressible amorphous polymers. Mechanics of Time-Dependent Materials, 14, pp. 261–275, (2010).

[17] Paggi, M., Sapora, A. An accurate thermoviscoelastic rheological model for ethylene vinyl acetate based on fractional calculus. International Journal of Photoenergy, 2015(1), pp. 252740, (2015).

[18] Lenarda, P., Paggi, M. A computational framework for rheologically complex thermo-visco-elastic materials. International Journal of Solids and Structures, 236, pp. 111297, (2022).

[19] Smyshlyaev, V. P., Cherednichenko, K. On rigorous derivation of strain gradient effects in the overall behaviour of periodic heterogeneous media. Journal of the Mechanics and Physics of Solids, 48(6), pp. 1325–1357, (2000).

[20] Smyshlyaev, V. P. Propagation and localization of elastic waves in highly anisotropic periodic composites via two-scale homogenization. Mechanics of Materials, R59, pp. 434–447, (2009).

[21] M.G.D. Geers, V. K., Brekelmans, W. Multi-scale computational homogenization: trends and challenges. Journal of Computational and Applied Mathematics, 234, pp. 2175–2182, (2010).

[22] Zäh, D., Miehe, C. Computational homogenization in dissipative electro-mechanics of functional materials. Computer Methods in Applied Mechanics and Engineering, 267, pp. 487–510, (2013).

[23] Wautier, A., Guzina, B. B. On the second-order homogenization of wave motion in periodic media and the sound of a chessboard. Journal of the Mechanics and Physics of Solids, 78, pp. 382–414, (2015).

[24] Hu, R., Oskay, C. Multiscale nonlocal effective medium model for in-plane elastic wave dispersion and attenuation in periodic composites. Journal of the Mechanics and Physics of Solids, 124, pp. 220–243, (2019).

[25] Lopes, I. A. R., Pires, F. M. A. An assessment of multi-scale models based on second-order computational homogenisation. Computers & Structures, 259, pp. 106679, (2022).

[26] Touboul, M., Vial, B., Assier, R., et al. High-frequency homogenization for periodic dispersive media. Multiscale Modeling & Simulation, 22(3), pp. 1136–1168, (2024).

[27] Liupekevicius, R., van Dommelen, J., Geers, M., et al. Equivalent continuum for viscoelastic metamaterials. Computer Methods in Applied Mechanics and Engineering, 445, pp. 118160, (2025).

[28] Chen, Z., Wu, B., Xie, Y. M., et al. Fft-based inverse homogenization for cellular material design. International Journal of Mechanical Sciences, 231, pp. 107572, (2022).

[29] Yang, H., Abali, B. E., Müller, W. H., et al. Verification of asymptotic homogenization method developed for periodic architected materials in strain gradient continuum. International Journal of Solids and Structures, 238, pp. 111386, (2022).

[30] Vazic, B., Abali, B. E., Newell, P. Generalized thermo-mechanical framework for heterogeneous materials through asymptotic homogenization. Continuum Mechanics and Thermodynamics, 35(1), pp. 159–181, (2023).

[31] Barceló-Mercader, J., Codony, D., Mocci, A., et al. Computational homogenization of higher-order electro-mechanical materials with built-in generalized periodicity conditions. Computer Methods in Applied Mechanics and Engineering, 423, pp. 116861, (2024).

[32] Li, B., Zhang, R., Żur, K. K., et al. Second-order computational homogenization of flexoelectric composites with isogeometric analysis. Computer Methods in Applied Mechanics and Engineering, 442, pp. 118031, (2025).

[33] Chen, Q., Du, X., Chatzigeorgiou, G., et al. Physics-informed deep neural networks towards finite strain homogenization of unidirectional soft composites. European Journal of Mechanics-A/Solids, p. 105752, (2025).

[34] Préve, D., Bacigalupo, A., Paggi, M. Variational-asymptotic homogenization of thermoelastic periodic materials with thermal relaxation. International Journal of Mechanical Sciences, 205, pp. 106566, (2021).

[35] Del Toro, R., De Bellis, M. L., Vasta, M., et al. Multifield asymptotic homogenization for periodic materials in

non-standard thermoelasticity. International Journal of Mechanical Sciences, 265, pp. 108835, (2024).

[36] Vlasov, A., Volkov-Bogorodsky, D., Savatorova, V. Using asymptotic homogenization in parametric space to determine effective thermo-viscoelastic properties of fibrous composites. In *Advances in Mechanics of Time-Dependent Materials*, pp. 153–171. Springer, (2023).

[37] Hirsekorn, M., Marcin, L., Godon, T. Thermo-viscoelastic homogenization of 3d woven composites with time-dependent expansion coefficients. International Journal of Solids and Structures, 244, pp. 111569, (2022).

[38] Huang, S., Qi, Y., Zhang, J., et al. Multiscale homogenization of thermo-mechanical viscoelastic response of 3d orthogonal composites with time-dependent ctes. Composite Structures, 347, pp. 118479, (2024).

[39] Kaku, K.-h., Arai, M., Fukuoka, T., et al. Evaluation of thermo-viscoelastic property of cfrp laminate based on a homogenization theory. Acta Mechanica, 214, pp. 111–121, (2010).

[40] Trofimov, A., Le-Pavic, J., Therriault, D., et al. An efficient multi-scale computation of the macroscopic coefficient of thermal expansion: Application to the resin transfer molding manufactured 3d woven composites. International Journal of Solids and Structures, 210, pp. 162–169, (2021).

[41] Hirsekorn, M., Marcin, L., Godon, T. Multi-scale modeling of the viscoelastic behavior of 3d woven composites. Composites Part A: Applied Science and Manufacturing, 112, pp. 539–548, (2018).

[42] Zhi, J., Yang, B., Li, Y., et al. Multiscale thermo-mechanical analysis of cure-induced deformation in composite laminates using direct fe2. Composites Part A: Applied Science and Manufacturing, 173, pp. 107704, (2023).

[43] Chen, W., Zhang, D. Improved prediction of residual stress induced warpage in thermoset composites using a multiscale thermo-viscoelastic processing model. Composites Part A: Applied Science and Manufacturing, 126, pp. 105575, (2019).

[44] Christensen, R. *Theory of viscoelasticity: an introduction*. Elsevier, (2012).

[45] Fantoni, F., Bacigalupo, A. Multifield constitutive identification of non-conventional thermo-viscoelastic periodic cauchy materials. International Journal of Mechanical Sciences, 223, pp. 107228, (2022).

[46] Del Toro, R., De Bellis, M. L., Bacigalupo, A. Design of a thermoelastic metafilter through non-local continualization methods. International Journal of Mechanical Sciences, 280, pp. 109483, (2024).

[47] Bacigalupo, A. Second-order homogenization of periodic materials based on asymptotic approximation of the strain energy: formulation and validity limits. Meccanica, 49(6), pp. 1407–1425, (2014).

[48] Del Toro, R., Bacigalupo, A., Lepidi, M., et al. Dispersive waves in magneto-electro-elastic periodic waveguides. International Journal of Mechanical Sciences, 236, pp. 107759, (2022).

[49] Del Toro, R., Fantoni, F., De Bellis, M. L., et al. A multiscale approach to visco-electro-elastic complex materials: Asymptotic homogenization versus high-frequency continualization schemes. International Journal of Engineering Science, 216, pp. 104331, (2025).